

A deep *WISE* search for very late type objects and the discovery of two halo/thick-disc T dwarfs: WISE 0013+0634 and WISE 0833+0052

D. J. Pinfield,^{1*} J. Gomes,¹ A. C. Day-Jones,^{1,2} S. K. Leggett,³ M. Gromadzki,⁴ B. Burningham,¹ M. T. Ruiz,² R. Kurtev,⁴ T. Cattermole,¹ C. Cardoso,⁵ N. Lodieu,^{6,7} J. Faherty,^{2,8} S. Littlefair,⁹ R. Smart,⁵ M. Irwin,¹⁰ J. R. A. Clarke,¹ L. Smith,¹ P. W. Lucas,¹ M. C. Gálvez-Ortiz,¹¹ J. S. Jenkins,² H. R. A. Jones,¹ R. Rebolo,^{6,7} V. J. S. Béjar^{6,7} and B. Gauza^{6,7}

¹Centre for Astrophysics Research, Science and Technology Research Institute, University of Hertfordshire, Hatfield AL10 9AB, UK

²Universidad de Chile, Santiago, Casilla 36-D, Chile

³Gemini Observatory, Northern Operations Center, 670 N. A'ohoku Place, Hilo, HI 96720, USA

⁴Departamento de Física y Astronomía Universidad de Valparaíso, Av. Gran Bretaña 1111, Playa Ancha, Casilla 5030, Chile

⁵Istituto Nazionale di Astrofisica, Osservatorio Astronomico di Torino, Strada Osservatorio 20, I-10025 Pino Torinese, Italy

⁶Instituto de Astrofísica de Canarias, E-38200 La Laguna, Spain

⁷Dept. Astrofísica, Universidad de La Laguna, E-38206 La Laguna, Tenerife, Spain

⁸Department of Astrophysics, American Museum of Natural History, Central Park West at 79th Street, New York, NY 10034, USA

⁹Department of Physics and Astronomy, University of Sheffield, Sheffield S3 7RH, UK

¹⁰Institute of Astronomy, Madingley Road, Cambridge CB3 0HA, UK

¹¹Centro de Astrobiología (CSIC-INTA), Ctra. Ajalvir km 4, E-28850 Torrejón de Ardoz, Madrid, Spain

Accepted 2013 August 1. Received 2013 July 31; in original form 2012 October 27

ABSTRACT

A method is defined for identifying late-T and Y dwarfs in *WISE* down to low values of signal-to-noise. This requires a *WISE* detection only in the *W2*-band and uses the statistical properties of the *WISE* multiframe measurements and profile fit photometry to reject contamination resulting from non-point-like objects, variables and moving sources. To trace our desired parameter space, we use a control sample of isolated non-moving non-variable point sources from the Sloan Digital Sky Survey (SDSS), and identify a sample of 158 *WISE* *W2*-only candidates down to a signal-to-noise limit of eight. For signal-to-noise ranges > 10 and $8-10$, respectively, ~ 45 and ~ 90 per cent of our sample fall outside the selection criteria published by the *WISE* team, mainly due to the type of constraints placed on the number of individual *W2* detections. We present follow-up of eight candidates and identify WISE 0013+0634 and WISE 0833+0052, T8 and T9 dwarfs with high proper motion (~ 1.3 and ~ 1.8 arcsec yr⁻¹). Both objects show a mid-infrared/near-infrared excess of $\sim 1-1.5$ mag and are *K* band suppressed. Distance estimates lead to space motion constraints that suggest halo (or at least thick disc) kinematics. We then assess the reduced proper motion diagram of *WISE* ultracool dwarfs, which suggests that late-T and Y dwarfs may have a higher thick-disc/halo population fraction than earlier objects.

Key words: surveys – brown dwarfs – stars: low-mass.

1 INTRODUCTION

Population studies of brown dwarfs (mass $< 0.075 M_{\odot}$; Baraffe et al. 2003) can provide crucial constraints on the low-mass extreme of the star formation process (e.g. Reipurth & Clarke 2001; Bate, Bonnell & Bromm 2002; Goodwin & Whitworth 2007;

Bonnell, Clark & Bate 2008; Machida, Inutsuka & Matsumoto 2009; Stamatellos & Whitworth 2009), through measurements of the luminosity and mass functions (e.g. Cruz et al. 2007; Metchev et al. 2008; Pinfield et al. 2008; Bastian, Covey & Meyer 2010; Burningham et al. 2010b, 2013; Reylé et al. 2010; Kirkpatrick et al. 2012; Lodieu, Deacon & Hambly 2012a), and sampling of the formation history (e.g. Day-Jones et al. 2013). Also, the cooling of brown dwarfs leads to a T_{eff} range that encompasses the lowest

*E-mail: d.j.pinfield@herts.ac.uk

mass stars and giant planets. As such, brown dwarfs make excellent test beds to improve our understanding of sub-stellar atmospheres (e.g. Pinfield et al. 2006, 2012; Burningham et al. 2009; King et al. 2010; Zhang et al. 2010; Day-Jones et al. 2011; Faherty et al. 2013; Gomes et al. 2013).

Brown dwarf discovery began in 1995 (Nakajima et al. 1995; Rebolo, Zapatero Osorio & Martín 1995), and has expanded, mainly through the use of large-scale surveys, into several new spectral classes. The 2MASS (Skrutskie et al. 2006), DENIS (Epchtein et al. 1999) and Sloan Digital Sky Survey (SDSS; York et al. 2000) surveys revealed the dusty L dwarfs (with $T_{\text{eff}} = 2300\text{--}1400\text{ K}$; e.g. Kirkpatrick et al. 1999), the methane-dominated T dwarfs (with $T_{\text{eff}} < 1400\text{ K}$; e.g. Strauss et al. 1999; Geballe et al. 2002; Burgasser et al. 2006) and the LT transition objects that join together these two spectral types (e.g. Leggett et al. 2000). More recently, the UKIDSS surveys and the Canada France Brown Dwarf Survey (CFBDS) have identified the coolest examples of the T dwarf class in the 500–700 K range (e.g. Warren et al. 2007; Burningham et al. 2008, 2010a; Delorme et al. 2008; Lucas et al. 2010), with large-scale deep near-infrared coverage. However, it took the mid-IR sensitivity of the *WISE* observatory (Wright et al. 2010) to break through into the $<500\text{ K}$ regime for free-floating field objects. Although *WISE* has a similar sensitivity to L dwarfs as 2MASS (thus providing good scope for infrared proper motion surveys; Castro, Gizis & Gagné 2011; Gizis et al. 2011a; Gizis, Troup & Burgasser 2011b; Castro & Gizis 2012), the relative dominance of mid-infrared emission for $<500\text{ K}$ objects (particularly around $4.5\ \mu\text{m}$; Burrows, Sudarsky & Lunine 2003; Mainzer et al. 2011; Allard, Homeier & Freytag 2012) leads to a greatly increased sensitivity at this T_{eff} .

Such objects are known as Y dwarfs. Like late-T dwarfs, Y dwarf spectra exhibit deep H_2O and CH_4 absorption bands which dominate their spectral morphology. However, the Y dwarf WISE 1828+2650 (Cushing et al. 2011, presented as the archetype) has notably extreme colours ($J - W_2 = 9.3$) and a spectrum that is markedly different to the latest T dwarfs (e.g. UGPS 0722–0540; Lucas et al. 2010). The $J - H$ colour of WISE 1828+2650 is much redder than those of the late Ts showing that a reversal of the previously known colour trend has occurred, indicative of a collapse in the near-infrared flux relative to that at $\sim 5\ \mu\text{m}$ (Cushing et al. 2011). Furthermore, the $[3.6] - [4.5]$ *Spitzer* colour shows a turn to the blue that may be indicative of a shift in position of the $\sim 5\ \mu\text{m}$ flux peak (Kirkpatrick et al. 2012, K12 hereafter). WISE 1828+2650 would thus seem to fulfil at least one of the five criteria put forward by Burrows et al. (2003) for the establishment of the Y class. Despite the marked difference between the late-T dwarfs and the archetypal Y dwarf, the actual transition follows a gradual change (as per the norm) which is predominantly quantified by the narrowness of the J -band flux peak (see also Mace et al. 2013).

In comparison to *WISE*, the UKIDSS Large Area Survey and Galactic Survey cover ~ 7000 square degrees of sky down to $J \sim 19.5$ (Lawrence et al. 2007), with VISTA now expanding into the southern sky (e.g. Gauza et al. 2012; Lodiou et al. 2012b). However, Y dwarfs generally have $J - W_2 \geq 5$, and the first *WISE* Y dwarfs were found in about half the sky in the $W_2 = 14\text{--}14.5$ range (Cushing et al. 2011; Kirkpatrick et al. 2011, K11 hereafter). From a Y dwarf perspective, the *WISE* W_2 coverage and sensitivity in the first incremental release was equivalent to a near-infrared survey reaching $J > 19.5$ over half the sky. Indeed, when considering the reddest Y dwarfs currently known (e.g. $J - W_2 \sim 9$) *WISE* is sensitive out to ~ 10 times the distance of the deepest near-infrared surveys.

The collaboration led by Kirkpatrick of the *WISE* Science team is implementing an ongoing search for late-T and Y dwarfs in *WISE* (K11; K12). Though maintaining a variety of candidate lists, their general search method has been characterized in K12. As well as a set of colour, magnitude and coordinate constraints, and allowances for non-detection in some bands, they placed constraints on a set of criteria parametrizing source detection and character. Thresholds were used for the number of detections in individual frames (to remove spurious aligned artefacts), blending with other sources was avoided (since it can result in poorly determined photometry) and the point-like nature of a source was assessed. This programme discovered the first Y dwarfs (Cushing et al. 2011), and has to-date identified a population of 14 objects in this new class (K12; Tinney et al. 2012).

In another *WISE* search, Pinfield et al. (2012) searched for wide companion late-T and Y dwarfs around Hipparcos and Gliese stars. This search had similar colour constraints and allowances for non-detection in various bands, but did not place any further constraints on source detection and character. This was a practical approach in this case because only candidate widely separated companions were taken forward for closer inspection, and the sky coverage was severely limited by the requirement for proximity to Hipparcos and Gliese stars. The distances of the possible primary stars also contributed to the assessment (since companions would be essentially at the same distance as their primary) and visual inspection could proceed for a few tens of candidates after an automated selection process. This search identified a new metal poor T8p companion, and recovered three other previously known objects (T6p, T8 and T8.5).

In this paper, we describe a new search method designed to effectively identify late-T and Y dwarf candidates in the full *WISE* sky down to a faint detection limit in W_2 . Sections 2.1–2.4 present our selection and rejection method, making use of a control sample to assess W_2 source characteristics. We initially search down to W_2 signal-to-noise of 10, and Section 2.5 extends our search down to a signal-to-noise of 8. We discuss our visual inspection process in Section 2.6, and the new candidate sample itself in Section 2.7. Section 3 describes a classification system that allows us to prioritize candidates for further follow-up, and Section 4 describes our current photometric follow-up measurements. Our analysis of the recently identified WISE 1639–6847 is presented in Section 6.1. And the two newly discovered objects WISE 0013+0634 and WISE 0833+0052 are discussed in Section 6.2. We plot and assess these new objects, and also other L T and Y dwarfs with measured proper motion, in reduced proper motion diagrams in Section 7. Future work is considered in Section 8.

2 CANDIDATE SELECTION

2.1 The initial selection

In typical *WISE* sky (10–30 exposures), the 10σ limit occurs at $W_2 = 15\text{--}15.7$ and the detection limits (2σ) in the other bands are $W_1 \simeq 17.6$, $W_3 \simeq 12.3$ and $W_4 \simeq 9$. *WISE* Y dwarf colours are $W_1 - W_2 > 3.9$, $W_2 - W_3 = 1.7\text{--}2.6$ and $W_2 - W_4 \simeq 5$, so in general we thus expect Y dwarfs around the W_2 10σ limit to be non-detections in the other bands. We thus began by selecting All-Sky catalogue sources that were detected with a signal-to-noise of at least 10 in the W_2 band ($w_2\text{snr} \geq 10$), but that were not detected in the W_1 , W_3 and W_4 bands ($w_1\text{snr} \leq 10$ or $w_3\text{snr} \leq 10$ or $w_4\text{snr} \leq 10$, meaning that the profile fit magnitude is a 95 per cent confidence upper limit or that the source is not measurable). We also required that there

was no 2MASS source within 3 arcsec of the *WISE* source, and at least eight individual exposures in each bands ($w*m \geq 8$). Wright et al. (2010) explain how the *WISE* mission design provides at least eight exposures over more than 99 per cent of the sky during a 6 month mission.

To minimize contamination from reddened objects, we removed sources towards reddened regions of sky. To estimate reddening, we used the online Galactic Dust Reddening and Extinction Calculator at the NASA/IPAC Infrared Science Archive, which computes line-of-sight interstellar extinction using the technique pioneered by Schlegel, Finkbeiner & Davis (1998). To reject stars with reddened $W1 - W2 > 2.0$, we aimed to exclude regions with $E(W1 - W2) \geq 1.4$ (since normal stars have $W1 - W2 = 0.0-0.4$ and will scatter somewhat in colour due to photometric uncertainty). This constraint was transformed into an A_v limit using the extinction curves of Mathis (1990) leading to a rejection criterion where the average line-of-sight visual extinction $A_v > 0.45$. We also allowed for extinction variation of 0.35 mag (due to dense structures) across the ~ 5 arcmin on-sky resolution of the extinction maps (this range of variations is exceeded in only ~ 1 per cent of the sky). We thus rejected sources towards regions of sky with average line-of-sight extinction $A_v > 0.8$ (21.7 per cent of the sky).

We experimented with the `ccflag` parameter to remove sources flagged as possible spurious detections of diffraction spikes, persistence, haloes or optical ghosts in the *W2* band. However, there was no such contamination in our initial selection, which consisted of 6067 sources with $w2snr \geq 10$.

2.2 Refining the selection

We devised a set of additional selection criteria to remove contamination in the form of (i) resolved (or partially resolved) sources such as galaxies and sources associated with nebulousity or artefacts, (ii) variable sources and (iii) sources that move significantly over the time-scale of the multiframe images (i.e. Solar system objects).

2.3 The control sample

As a means to differentiate between the desired data base properties of quality sources and those of contamination that we wish to reject, we defined a control sample of isolated point-like non-variable non-moving sources, extending all the way down to the faint survey limits. To define this control sample, we combined the SDSS with *WISE*. We selected sources spectroscopically classed by SDSS as stars, and to avoid field crowding (and thus prefer isolated sources) we limited our search to a galactic latitude $|b| > 70^\circ$ (also removing giant stars that could be variable). We used photometric limits of $g < 20.0$ and $g - r < 0.3$ to select stars with reasonably blue colour and *WISE* magnitudes down to $W2 = 18$. We selected point-like Sloan sources (that were un-blended in *WISE*) with proper motions $> 20 \text{ mas yr}^{-1}$ which we cross-matched with *WISE* using a 1 arcsec cross-match radius to avoid mismatches. We thus exclude non-moving galaxies and high proper motion objects, with the control sample thus consisting of stellar point sources that are stationary across the *WISE* multiframe measurements.

2.4 Rejection methods

In Fig. 1, the plots on the left-hand side show the control sample (small black points), as well as sources from the All-Sky late-T and Y dwarf census of K12 as blue symbols, except for Y dwarfs which are green. We plot our final selection of new candidates with

$w2snr > 8$ in red (see Section 2.5 for the $w2snr = 8-10$ selection). The plots on the right-hand side of Fig. 1 show how contamination is rejected from the 6067 *W2*-only initial selection with $w2snr > 10$. The rejection criteria that we employed are indicated with solid lines, and discussed below.

The top plots show our ‘profile fit photometry rejection method’ which assesses how point-like each source is. The `w2rchi2` parameter is plotted against $\log(w2snr)$, where $w2snr$ is the signal-to-noise of the *W2* measurements. `w2rchi2` is the reduced χ^2 of the *W2* profile fit photometry, and is a direct indicator of how well the source is represented by the optimized point spread function (PSF) fit. It can be seen from the control sample plot (top left) that in all but a small number of outlier cases (~ 1 per cent), `w2rchi2` lies in a band between 0.7 and 1.2 for $w2snr$ from 2 to 50 ($\log(w2snr) = 0.3-1.7$). Seven of the K12 census (~ 4 per cent) have `w2rchi2` > 1.2 , and visual inspection showed that the majority were very close to or slightly overlapping with neighbouring sources in the *WISE* images (although they are listed as unblended in the *WISE* data base). In these cases, this effect has led to an increased `w2rchi2` value for the profile fit photometry. We also note that in a few cases there was no clear explanation for the increased `w2rchi2` values, and these sources could warrant further study for unresolved multiplicity (e.g. Gelino et al. 2011; Liu et al. 2011). This rejection method should thus be effective at retaining isolated point sources, but will reject a small fraction where field crowding and blending are an issue.

The middle plots show our ‘photometric uncertainty rejection method’. We plot $\log(w2sigp1 - w2sigmpro)$ against $\log(w2snr)$, where `w2sigmpro` is the integrated flux uncertainty and `w2sigp1` is the standard deviation of the population of *W2* fluxes measured on the individual frames (both in magnitude units). For isolated non-variable non-moving objects, `w2sigp1` provides a direct measure of the uncertainty on individual frames, which should relate to the integrated flux uncertainty. Indeed, the control sample (middle-left plot) traces out a well-defined sequence over the full signal-to-noise range, though there are two K12 sources (~ 1 per cent of the census) slightly above this sequence. However, visual inspection once again showed that these two sources slightly overlapped with neighbouring sources in the *WISE* images, which has led to an increase in the `w2sigp1` values. Guided by the control sample we rejected all sources that lie above the upper limit line in the plot, $\log(w2sigp1 - w2sigmpro) = 1.3 - 1.38 \log(w2snr)$.

The bottom plots show the ‘detection number rejection method’ that we used when there were a limited number (< 8) of detections in the individual frames. The plots show the fraction of individual *W2* frames in which the source was detected with a signal-to-noise greater than 3 (i.e. $w2nm/w2m$), against $\log(w2snr)$. The control sample traces out a sequence in this parameter-space (bottom-left plot), ranging from detection in all frames down to no individual detections (above a signal-to-noise of 3). We thus define a minimum fraction of frames in which the *W2* source must be detected, shown by the solid line where its sloping portion is defined by $w2nm/w2m < 1.8 \log(w2snr) - 1.7$. Although 11 of the K12 census (6 per cent) lie below this line, all 11 are detected in at least eight *W2* exposures and thus would not be rejected by our method. However, this is an indication of what could be rejected amongst sources detected in < 8 frames. Visual inspection showed that these outliers were all close to or overlapped with neighbouring sources in the *WISE* images, which clearly affects the ability of the *WISE* source detection algorithm to identify the source in individual frames. We therefore expect a low level of incompleteness (mostly in crowded fields) due to this rejection method. We rejected sources that were detected in less than eight frames if they lay below the rejection line.

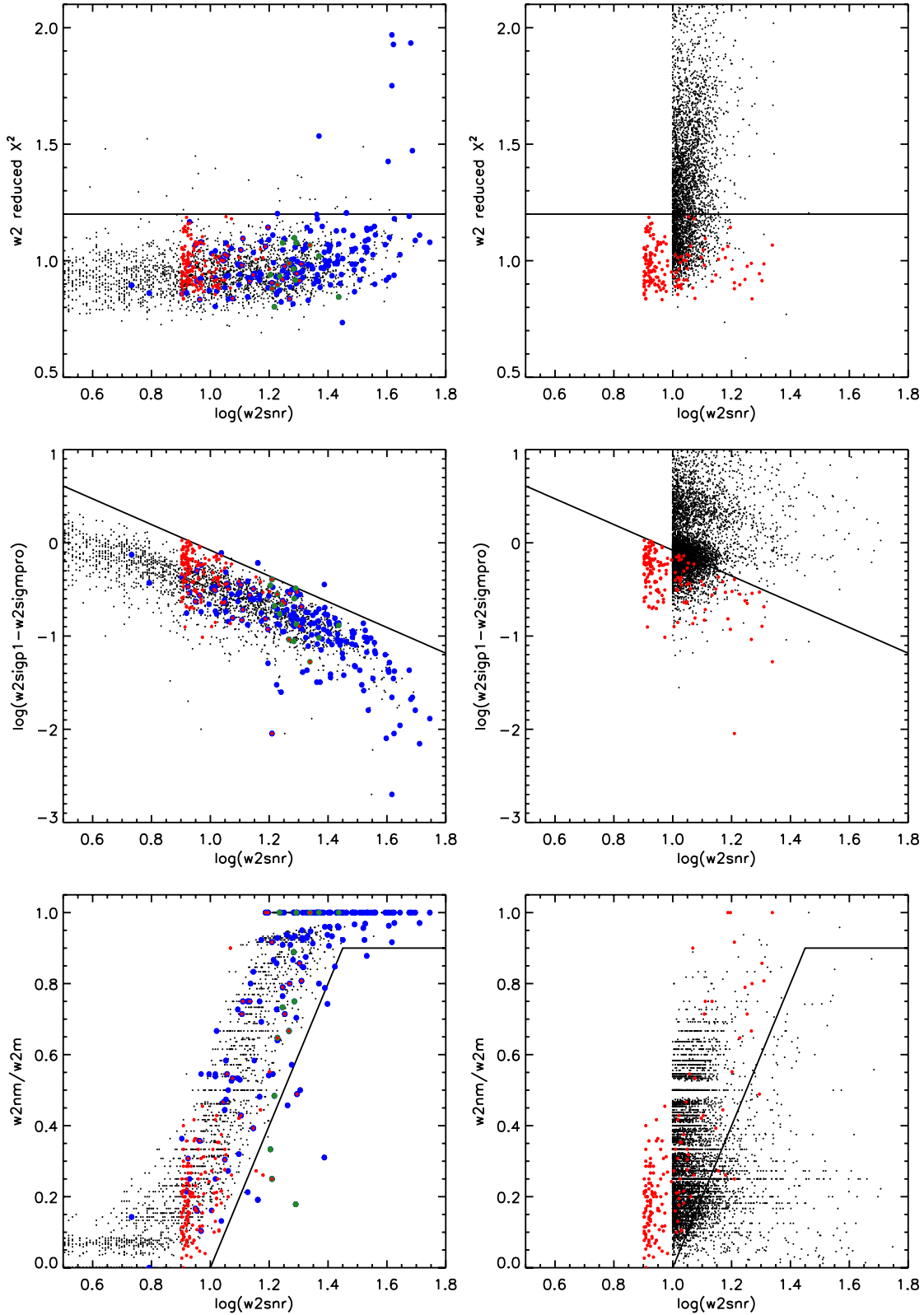


Figure 1. The plots show the three rejection methods employed by our search, which focus on assessing the profile fit photometry, the photometric uncertainties and the detection numbers. Plots on the left-hand side show the control sample (see text), as well as the K12 census (blue, except for Y dwarfs which are green). Plots on the right show our initial $w2snr > 10$ selection (small black symbols). Our rejection cuts are indicated with solid lines, and our final candidates are overlotted as red symbols.

Table 1. Summary of how the three main rejection methods incrementally reduce the initial $w2snr \geq 10$ selection. psf refers to the profile fit photometry rejection method, sig to the photometric uncertainty rejection method and det to the detection number rejection method.

w2snr ≥ 10 selection			
Initial selection: 6067			
Applied 1st			
	psf	sig	det
	1394	2804	5168
Applied 2nd			
psf	–	923	1342
sig	923	–	2483
det	1324	2483	–
After psf/sig/det rejections: 904			

Table 1 summarizes the number of $w2snr > 10$ candidates that remain after rejection using our three different methods. Results are shown for different orders of applying the methods, to indicate their effectiveness and highlight common ground amongst the rejection methods. It can be seen that the profile fit photometry method rejects the most objects, followed by the photometric uncertainty rejection method. It is also clear that the profile fit photometry method rejects most of the sources rejected by the detection number method. So the overall approach might be simplified without substantially reducing the number of rejected sources, by omitting the detection number method. However, we chose to apply all three methods here, rejecting 5163 sources and leaving 904 $w2snr > 10$ sources for visual inspection.

2.5 Extending the search to the 8σ W2 limit

We built on our $w2snr > 10$ selection by extending our analysis into the $w2snr = 8-10$ range. We made an initial selection of 18 112 sources, and our three rejection methods (from Section 2.4) left 3252 sources. A visual inspection of ~ 100 of these revealed that many were found close to bright stars, and resulted from spurious or poor quality detections within the extended bright star haloes. We therefore implemented an additional rejection method for this $w2snr$ range, to remove such contamination prior to visual inspection. The contamination and confusion flag (`cc_flags`) parameter in the All-Sky Database assesses such contamination, though we chose to establish our own halo criterion so as to optimize this rejection method for our sample.

Fig. 2 shows a zoomed in plot of the separations between our 3252 sources and their nearest bright 2MASS neighbour (where J_{2MASS} is the 2MASS J -band magnitude of the bright object). The full range of separation extends out to $\sim 10\,000$ arcsec, but it can be seen that a large number of candidates are found within about 600 arcsec of a bright star if its magnitude is $J_{2MASS} \leq 3.5$. This overdensity (1590 sources) clearly identifies the separation–brightness region where halo contamination is common amongst our $W2$ -only $w2snr = 8-10$ sources. For comparison we overplot (in orange) the 946 sources that are flagged as halo associations in the *WISE* data base, and it is clear that the *WISE* data base does not account for all of the $W2$ -only contamination around bright stars. We therefore removed any $w2snr = 8-10$ sources that are close to a bright 2MASS star with $J_{2MASS} \leq 3.5$ if their separation (s) from this star fulfils the criterion $s \leq (-157.14 \times J_{2MASS}) + 850$ (shown by the solid line

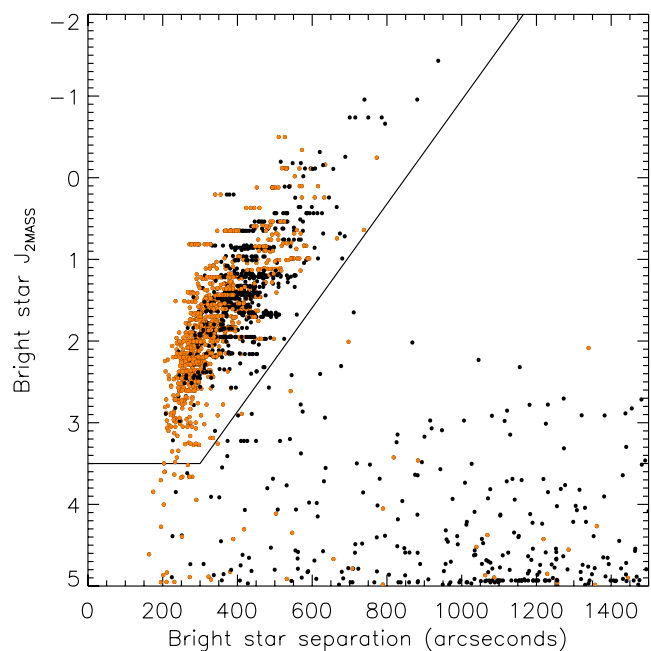


Figure 2. The separation between $W2$ -only sources and their nearest bright 2MASS neighbour. Overplotted in orange are sources flagged as halo associations in the *WISE* All-Sky release data base. The solid line delineates our own halo rejection region.

in Fig. 2). This criterion removed about half of the 3252 $W2$ -only sources, which were found in only 193 square degrees (0.5 per cent) of sky around bright stars.

2.6 Visual inspection

We used the *WISE* Image Service at the NASA/IPAC Infrared Science Archive to examine candidate $W2$ -only sources that came through both our selections ($w2snr > 10$ and $w2snr = 8-10$). We visually examined 600 arcsec Atlas images in all four *WISE* bands, but made use of the zoom and background image stretch settings in some cases. We assessed the quality of sources in several ways. We rejected sources that were associated with artefacts, including diffraction spikes, optical ghosts, glints, spurious halo associations and some sources in regions with a poorly fit sky (which can result from latents). Next we compared the $W2$ sources with noise features in the local sky, and visually assessed their shape for point source consistency. We thus rejected many sources that were part of resolved extended structure such as nebulosity and galaxies. We also rejected visually blended sources if the blending precluded reasonable quality assessment in other respects. And we rejected sources with visual counterparts in the $W1$, $W3$ or $W4$ bands. In some cases the presence of such counterparts was unambiguous, though in others we had to assess significance relative to noise features in the local sky.

We also used the *WISE* 3-Band Cryo data release to examine a second epoch of imaging data. 3-Band Cryo data were acquired by *WISE* following the exhaustion of solid hydrogen in the satellite’s payload outer cryogen tank, and covers 30 per cent of the sky. Where available this data provide an additional Atlas image epoch ~ 6 months after the All-Sky measurement. This allowed us to perform the same visual assessments on a second epoch of data, and also examine the two $W2$ epochs for any evidence of proper motion. While the spatial resolution of *WISE* is low [the $W2$ full

width-half-maximum (FWHM) is 6.4 arcsec, and *WISE* Atlas Images have 1.375 arcsec per pixel] nearby objects with proper motion of 2.5–3 arcsec per year could move by \sim a pixel between the two epochs, and may thus be identified through visual inspection. We rejected nine sources which looked spurious in the extra epoch image.

2.7 The new sample

In all we have identified 158 *W2*-only sources, 52 with $w2snr \geq 10$ and 106 with $w2snr = 8-10$. 28 of these sources are previously identified T5-Y dwarfs from the literature (24 $w2snr \geq 10$ and 4 with $w2snr = 8-10$; K12; Burningham et al. 2010b; Lodieu et al. 2012b). 24 of the re-identified objects are previous *WISE* discoveries from the *WISE* census summarized by K12, so to provide a more in-depth comparison with this work we filtered our sample using the K12 selection criteria. In total 37 of our sample pass the K12 selection criteria and 121 do not. For those that do not, Table 2 summarizes the reasons.

None of our sample are rejected by the K12 $W1 - W2 > 2$ or $W2 - W3 < 3.5$ criteria, unsurprising since we are considering *W2*-only sources. None of our sources are flagged as artefacts, and the K12 Galactic plane ('GP') exclusion region covers significantly less sky (240 square degrees) than our $A_v < 0.8$ criterion (8952 square degrees). Our constraints on the reduced χ^2 of the *W2* profile fit photometry are substantially tighter than those of K12 (see Section 2.4), so none of our sources are rejected by this K12 criterion. And the K12 '<20 pc' criterion does not affect our sample because our sources only have lower limit $W1 - W2$ colours.

A small fraction of our sources fail the K12 blending requirement. However, the K12 criterion that affects our sample the most is the 'detection' criterion – K12 required that a source must have at least eight detections ($\geq 3\sigma$) in the individual *W2* frames, or where there

are 5–7 detections it must be detected in at least 40 percent of the *W2* frames. 87 percent of our $w2snr > 10$ sources (and all the $w2snr = 8-10$ sources) that are rejected by the K12 criteria failed to meet the K12 detection criterion.

Fig. 3 plots the new sample (red symbols) in *W2* versus $W1 - W2$ and $W2 - W3$ colour–magnitude diagrams. Y dwarfs (from K12 and Tinney et al. 2012) are green, with other K12 sources blue. Triangles indicate lower and upper limit colours, pointing to the right and left, respectively. The dotted lines indicate the 5σ and 2σ *W1* and *W3* limits (assuming 20 frames) in the left and right-hand plots, respectively. The limit colours become common in the 2–5 σ region, and dominate at fainter magnitudes.

Where our search has re-identified K12 objects the red symbols can be seen nested within the blue/green symbols. We re-identify 25 of the 33 *W2*-only detected K12 objects, with 5 being in $A_v > 0.8$ directions, 1 each being rejected by our profile fit photometry and photometric uncertainty rejection methods (see Section 2.4 and Fig. 1), and 1 having $w2snr < 8$. Of the 14 Y dwarfs 1 has a measured *W1* magnitude in the All-Sky data base due to an erroneous de-blending procedure as noted by K12, and 8 are detected in *W3*. Most of these *W3* detections lie around the indicated *W3* detection limit (shown in the right-hand plot), and indeed their *W3* photometric uncertainties range from 0.2 to 0.5. However, three of these *W3*-detections are markedly below these lines because there are > 30 frames of coverage for these objects (the faintest one being covered by 84 frames). Four of the five *W2*-only Y dwarfs are re-identified by our search method, with the fifth one being in an $A_v > 0.8$ direction.

The brightest object in our new sample is WISE 1639–6847, a blended source with $W2 = 13.64$. This is the brightest (in *W2*) Y dwarf known, and was recently discovered by Tinney et al. (2012) just prior to the submission of this paper. We discuss our own analysis of this object in Section 6.1. In the $W2 = 14-15$ range we identify 16 sources, 15 of which are previously known late-T and Y dwarfs and 2 of which are rejected by the K12 selection method. The dominant magnitude range for the new sample is $W2 = 15-16$, where we find 116 sources. 13 of these are previously reported objects, with 95 being rejected by the K12 selection method. Our sample also contains 25 sources fainter than $W2 = 16$, 14 of which are rejected by the K12 method.

3 CANDIDATE CLASSIFICATION

Our candidate sample will contain many mid–late T dwarfs as well as a smaller number of Y dwarfs, and we carry out our near-infrared imaging follow-up so as to classify such objects, as well as to weed out spurious candidates. The majority of late objects in our sample will be T dwarfs, and their blue $J - H$ colour means it is faster overall to search for near-infrared counterparts in the *J* band. To guide this process we considered the expected photometry and proper motion that our candidates should have if they are T or Y dwarfs with disc or thick-disc/halo kinematics. T5-8 dwarfs typically have $J - W2 = 2-4$, with T9s redder at $J - W2 = 4-6$ (e.g. K11). The known Y dwarfs all have $J - W2 > 4$ (the bluest one to date having $J - W2 = 4.32 \pm 0.26$) and their $J - W2$ can be extremely red (e.g. $J - W2 = 9.19 \pm 0.36$). Y dwarfs have $M_{W2} > 14.5$ (see fig 13 of K12), and we thus expect Y dwarfs in our sample (with $W2 = 15-16$ in our sample) to have distances < 20 pc. Mid–late T dwarfs have $M_{W2} < 14$ and will thus generally be beyond ~ 16 pc (for $W2 = 15-16$). For distances beyond 16 pc and with a typical disc velocity dispersion of 25–50 km s $^{-1}$ (for 1–5 Gyr, e.g. Griv, Gedalin & Eichler 2009), we expect T dwarf proper

Table 2. Summary of how the new sample selection criteria map on to the K12 criteria. 'Detections' refers to the required number of detections in individual frames. 'Blended' refers to the requirement that a source is not blended with another source. 'Profile' is the constraint placed on the quality of the profile fit photometry. 'GP' refers to the Galactic plane exclusion region and '<20 pc' refers to the colour–magnitude constraints designed to remove objects beyond a distance of 20 pc.

	New sample	
	$w2snr \geq 10$	$w2snr = 8-10$
Total	52	106
Retained by	29	8
K12 criteria	–	–
Rejected by	23	98
K12 criteria	–	–
Why rejected?	–	–
$W1 - W2 > 2$	0	0
Detections	21	98
$W2 - W3 < 3.5$	0	0
Artefact	0	0
Blended	3	0
Profile	0	0
GP	0	0
<20 pc	0	0

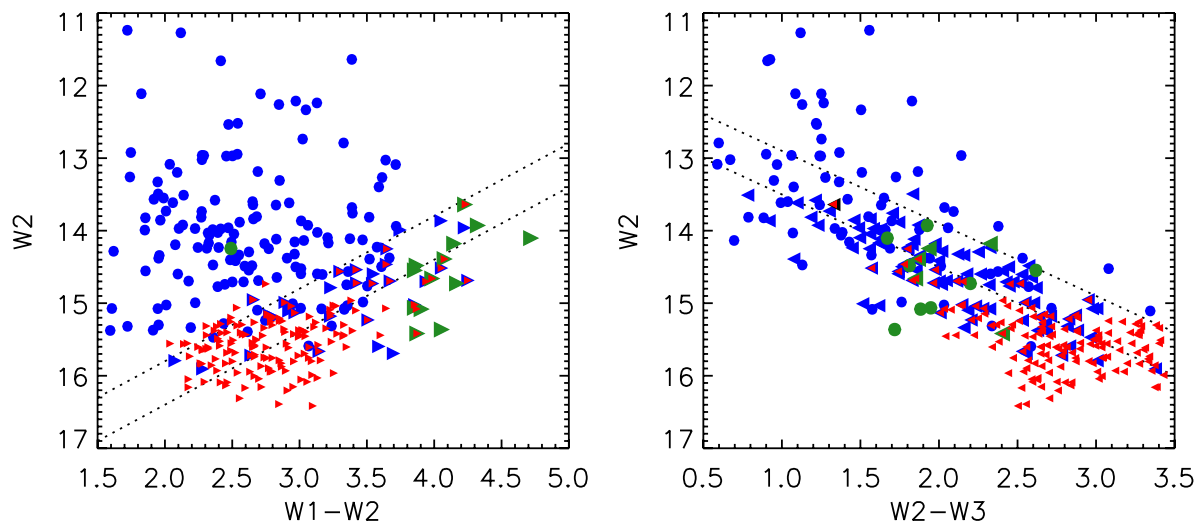


Figure 3. *WISE* $W2$ against $W1 - W2$ and $W2$ against $W2 - W3$ colour–magnitude diagrams. Our new sample is shown with red symbols (triangles point away from the lower limit colours). Objects from the K12 census are also shown (blue, except for Y dwarfs which are green). Dotted lines show the 5σ and 2σ $W1$ and $W3$ limits (assuming 20 frames).

Table 3. Candidate classification using near-infrared colour and proper motion.

Category	$J - W2$	μ_{tot} (arcsec yr $^{-1}$)	Interpretation
1	2–4	<0.7	Mid–late T (disc)
2	2–4	>0.7	Mid–late T (thick-disc/halo)
3	4–6	<0.3	Late T (disc)
4	4–6	0.3–0.7	Late T or Y (disc)
5	4–6	>0.7	Late T (thick-disc/halo) or Y
6	>6	<0.7	Low μ Y
7	>6	>0.7	Clear Y

motions of <0.7 arcsec yr $^{-1}$. With distances <20 pc Y dwarfs will generally have proper motion >0.3 arcsec yr $^{-1}$, though in some rare cases e.g. where their velocity is mostly along the line of sight, their proper motion could be smaller. Bringing this information together we defined some representative candidate classification categories to help us prioritize based on follow-up measurements of detected J -band counterparts. These categories are summarized in Table 3.

To assess the credence of possible J -band counterparts of our *WISE* candidates, we considered on-sky densities of J -band sources. A search of VISTA Hemisphere Survey (VHS) reveals ~ 0.01 sources with $J = 17.5\text{--}20.2$ per 7 arcsec 2 (equivalent to a circular sky area of radius 1.5 arcsec) in directions away from the Galactic plane. It is therefore very unlikely to find mismatched counterparts in this separation and magnitude range, and we thus assume any such counterparts to be genuine. *WISE* astrometric accuracy ranges from 0.28 to 0.44 arcsec for $W2$ -only sources with $w2_{\text{snr}} = 8\text{--}15$ (using Zacharias et al. 2010; Wright et al. 2010), so sources within 1.5 arcsec of the *WISE* position will have moved no more than 2 arcsec between the *WISE* and near-infrared epochs, and with typical baselines of a few years such sources will generally be in categories 1, 3, 4 or 6 (see Table 3).

At larger offsets mismatched near-infrared counterparts become more likely, e.g. we find ~ 0.6 VHS sources with $J = 17.5\text{--}20.2$ per 314 sq arcsec (equivalent to a 10 arcsec circle of sky). We routinely check SuperCOSMOS and SDSS (where available) to assess possible offset counterparts. However, such faint sources are gen-

erally non-detections in these surveys. It is therefore important to verify widely offset counterparts through additional epoch images (showing the proper motion) or multiband photometry giving near-infrared colour criteria, before assigning them to category 2, 5 or 7. If no near-infrared counterpart is detected, the candidate cannot be classified using Table 3, and additional mid-infrared follow-up will then be required.

4 ADDITIONAL PHOTOMETRY AND PROPER MOTIONS

We used the WFCAM Science Archive and the VISTA Science Archive (run by the Wide Field Astronomy Unit at the Institute for Astronomy, Royal Observatory Edinburgh) to search for available near-infrared imaging of our sample in Data Release 9 of the UKIDSS surveys (Lawrence et al. 2007), as well as the VHS (McMahon and the VHS Collaboration, in preparation) and VISTA VIKING survey (Findlay et al. 2012). We also searched the United Kingdom Infrared Telescope (UKIRT) Hemisphere Survey (UHS; a UKIDSS follow-on survey), taking advantage of pipeline processing and fast access to the data provided by the Cambridge Astronomical Survey Unit. These UKIRT and VISTA surveys reach $J = 20.2$ and $J = 20.9$, respectively. In this way, we obtained near-infrared imaging for three new candidates from the UKIDSS LAS, eight new candidates from the VHS, and seven new candidates from UHS. We also obtained J -band imaging of four candidates and H -band imaging of one candidate with the Four Star instrument on the 6.5 m Magellan Baade Telescope at Las Campanas Observatory, Chile. We measured J -band images of seven candidates with the Near-Infrared Camera Spectrometer (NICS) instrument on the 3.58 m Telescopio Nazionale Galileo (TNG) at Roque de los Muchachos Observatory on La Palma in the Canary Islands. In addition, we obtained J - and H -band images of two candidates with the HAWK-I instrument on the European Southern Observatory (ESO) Very Large Telescope (VLT). We measured 17 candidates using the Son of ISAAC (Sofi) instrument on the ESO New Technology Telescope. This data provide follow-up for 45 candidates, though here we only report on the candidates we have been able to confirm (i.e. classify according to Table 3).

Four Star observations were obtained on 2012 August 10. Images were taken with the *J*-band filter (MKO system), using individual integrations of 20 s, with six co-adds and a random 11-point jitter pattern, leading to total exposure times of 22 min. The target was centred on detector 2 as it has the most uniform pixel sensitivity, providing a 5.4 arcmin field of view (FOV). The data were reduced using standard IRAF routines.

NICS (Baffa et al. 2001) observations were made on the nights of 2012 August 2, 3 and 5. Image mosaics were produced by combining individual exposures of 30 s, with two or four co-adds, and five different pointings giving a total exposure time of 5 or 10 min. The mosaics were produced using the reduction Speedy Near-infrared data Automatic Pipeline (SNAP) provided by TNG. The TNG *J*-band filter is somewhat different to MKO *J*, so to determine a correction we derived synthetic photometry on the two systems. For standard stars (from the Pickles spectral library; Pickles 1998), we found essentially no difference between the different *J*-band magnitudes at a level of <0.4 per cent, and could thus use the transforms of Carpenter (2001) to convert 2MASS *J* into TNG *J*. For mid–late T dwarfs, however, we found a significant difference. We derived synthetic photometry using spectra of mid–late T spectral standards from Burgasser et al. (2006), and determined that $(J_{\text{TNG}} - J_{\text{MKO}}) = 0.55 \pm 0.08$.

HAWK-I observations were obtained on the nights of 2012 October 18 and 19 on the UT4 telescope on Paranal, Chile. HAWK-I is equipped with four Hawaii 2RG 2048×2048 pixel detectors and an MKO filter set which matches the VISTA filter set precisely (Kissler-Patig et al. 2008). In the *J*-band, five 60 s exposures were taken, with a random offset of up to 20 arcsec between them. The *H*-band data consisted of nine 100 s exposures, randomly offset from each other by up to 20 arcsec. Data reduction was carried out using the HAWK-I pipeline (V1.8.9) provided by ESO.

SoFI observations were obtained on 2012 December 31 under photometric conditions, seeing ~ 0.8 arcsec, and dark conditions. SoFI is equipped with a 1024×1024 Hawaii HgCdTe offering an FOV of 4.9×4.9 arcmin and a pixel size of 0.292 arcsec in its ‘Large-field’ configuration. *J*-band images were measured using integrations of 10 s repeated six times with a 10-point dither pattern yielding a total exposure of 10 min. Dome flats were obtained during the afternoon preceding the observations. The images were reduced with the ESO package GASGANO.

Warm-*Spitzer* IRAC photometry was obtained for two of the dwarfs presented in this work via Cycle 8 GO programme 80077 (PI: Leggett). The observations were carried out in both the [3.6] and [4.5] bands, with a 30 s frame time, repeated one to four times per pointing, and dither patterns consisting of 12, 16 or 36 positions. Post-basic-calibrated-data mosaics generated by the *Spitzer* pipeline version S19.1.0 were used to obtain aperture photometry

using a 7.2 arcsec diameter aperture, and the sky levels were determined from annular regions. Aperture corrections were taken from the IRAC handbook, and a 3 per cent uncertainty (due to systematics) contributes in quadrature to overall uncertainty. The *Spitzer* observations and photometry are summarized in Table 6.

We derived proper motions using a combination of near-infrared follow-up and *WISE* images, using multi-epoch near-infrared images where available. When we used a *WISE* epoch, we required near-infrared counterparts within ~ 1.5 arcsec of the *WISE* position, and that the *WISE* source was isolated and visually unblended to ensure reliable measurements. We typically selected 12–20 reference stars to define our interepoch positional transforms, which had root-mean-square residuals of ~ 0.03 – 0.07 arcsec. *J*-band counterpart centroiding uncertainties were estimated as a function of signal-to-noise, from the scatter in centroid measurements of a simulated population of sources with Gaussian PSF and added Poisson noise. Fit residuals and centroiding uncertainties were combined in quadrature to give full proper motion uncertainties.

To date we have been able to assign categories to eight new candidates using our *J*-band follow-up classification method. Six have *J*-band counterparts within 1.5 arcsec of the *WISE* source centre, and two have high proper motion near-infrared counterparts. *Spitzer* photometry was obtained for the two high proper motion objects. The follow-up photometry, assigned categories and proper motion measurements are presented in Tables 4–6. Near-infrared measurements of the other followed up candidates cannot be presented at this stage because in general we have identified possible counterparts and we need an additional measurement to confirm or reject them.

5 SPECTROSCOPY

Low-resolution near-infrared spectroscopy of *WISE* J001354.39+063448.2 (*WISE* 0013+0634 hereafter) and *WISE* J083337.83+005214.2 (*WISE* 0833+0052 hereafter) were obtained using the Gemini Near Infrared Spectrograph (GNIRS; Elias et al. 2006) on the Gemini North Telescope on Mauna Kea, Hawaii, and the Folded port InfraRed Echellette (FIRE) spectrograph (Simcoe et al. 2008, 2010) mounted on the Baade 6.5 m Magellan telescope at Las Campanas Observatory, respectively. The FIRE and GNIRS observations were made on the nights of 2013 February 14 and June 25 in clear conditions.

GNIRS observations were made via queue programme GN-2013B-Q-65. A 0.68 arcsec slit was used in cross-dispersed mode providing a 0.9–2.5 μm spectrum with a resolving power of $R \sim 750$. Eight 300 s integrations were obtained using an ABBA jitter pattern giving a total integration of 40 min. Comparison argon arc frames were obtained to provide dispersion solutions. For telluric

Table 4. Photometry of new late object discoveries. Mid-infrared limit colours are also given where one band has only a 95 per cent confidence upper limit magnitude. The object category is listed in the last column based on colour and proper motion (see Table 3).

Object	W2	W1 – W2	W2 – W3	<i>J</i> – W2	<i>H</i> – W2	<i>J</i> – <i>H</i>	<i>Y</i> – <i>J</i>	Category
<i>WISE</i> J001354.39+063448.2	15.04 ± 0.11	>3.27	<2.44	4.71 ± 0.12	4.98 ± 0.12	–0.28 ± 0.07		5
<i>WISE</i> J024345.58–021326.5	15.21 ± 0.10	>2.85	<2.25	2.50 ± 0.16				1
<i>WISE</i> J034019.34–003702.4	15.26 ± 0.12	>2.67	<2.65	3.68 ± 0.15			0.97 ± 0.21	1
<i>WISE</i> J041657.61–472115.0	16.17 ± 0.13	>2.60	<2.53	2.41 ± 0.14				1
<i>WISE</i> J083337.83+005214.2	14.96 ± 0.10	>3.39	<2.40	5.32 ± 0.14	5.67 ± 0.14	–0.35 ± 0.14	0.15 ± 0.24	5
<i>WISE</i> J132116.09–100512.3	15.72 ± 0.14	>3.00	<2.50	3.73 ± 0.19			1.34 ± 0.33	1 or 2 ^a
<i>WISE</i> J140143.50+394235.2	15.44 ± 0.10	>3.33	<2.22	2.90 ± 0.16				1
<i>WISE</i> J210216.60–272828.8	15.36 ± 0.14	>2.88	<2.80	2.40 ± 0.15	2.85 ± 0.18	–0.45 ± 0.13	1.53 ± 0.11	1 or 2 ^a

^aAmbiguous due to lack of proper motion constraint.

Table 5. Proper motion and reduced proper motion for late-type objects discussed in this paper.

Object	Facility (epoch 1 & 2)	Band	Obs date	$\mu_{\alpha\cos\delta}$ (arcsec yr ⁻¹)	μ_{δ} (arcsec yr ⁻¹)	RPM _{W2} ^a
WISE 0013+0634	UKIDSS LAS	<i>J</i>	2008-11-15	+1.17 ± 0.09	-0.54 ± 0.09	20.60
	Magellan	<i>J</i>	2012-08-10			
WISE 0243-0213	WISE-All-Sky	W2	2010-01-25	+0.21 ± 0.41	-0.03 ± 0.39	-
	TNG	<i>J</i>	2012-08-03			
WISE 0340-0037	UKIDSS LAS	<i>J</i>	2005-10-26	+0.00 ± 0.06	-0.03 ± 0.06	-
	VISTA VHS	<i>J</i>	2011-01-03			
WISE 0416-4721	WISE-All-Sky	W2	2010-01-29	-0.27 ± 0.03	+0.19 ± 0.03	18.76
	NTT	<i>J</i>	2012-12-31			
WISE 0833+0052	UKIDSS LAS	<i>J</i>	2006-12-11	+0.86 ± 0.04	-1.68 ± 0.04	21.34
	VLT	<i>J</i>	2012-10-18			
WISE 1401+3942	WISE-All-Sky	W2	2010-06-26	-0.27 ± 0.36	0.08 ± 0.37	-
	TNG	<i>J</i>	2012-08-06			
WISE 1639-6847	WISE-All-Sky	W2	2010-03-10	-0.8 ± 1.2 ^b	-2.8 ± 1.2 ^b	20.80
	WISE-3BC	W2	2010-09-06			

^aRPM is presented where proper motion is inconsistent with zero.

^bSee Tinney et al. (2012) for more accurate proper motions.

Table 6. *Spitzer* IRAC Photometry of new late object discoveries.

Object	Date observed	Integration time (s)	[3.6]	[4.5]	[3.6]–[4.5]
WISE 0013+0634	2013-02-12	1440	17.15 ± 0.03	15.16 ± 0.03	1.99 ± 0.04
WISE 0833+0052	2013-01-03	1440	17.02 ± 0.03	14.80 ± 0.03	2.22 ± 0.04

correction, the F5V star HD 5892 was observed after the target and at a similar airmass. Data reduction was carried out using standard IRAF GEMINI packages (Cooke & Rodgers 2005). Hydrogen lines were removed from the F5V stellar spectrum using linear interpolation, and the true continuum determined using the IRTF Spex library spectrum of HD 27524 (Rayner, Cushing & Vacca 2009).

The FIRE instrument was used in prism mode with a 0.6 arcsec slit giving a resolving power of $R \sim 200$ at 1.6 μm . Thirty 120 s integrations were obtained using an ABBA jitter pattern, giving a total integration of 1 h. Ne–Ar arc lamps were observed at the configuration and pointing for both the target and the standard to allow for good dispersion correction. Due to some saturation with the on-night standard calibration star, we made use of calibrators from 2012 October 5 and June 3. These nights had similar conditions to that of our target observation, and the standards were observed at a similar airmass. To verify the effectiveness of this approach, we generated four output spectra of WISE 0833+0052 using the four measured standards in order to compare the results and assess consistency. We found ≤ 10 per cent variation in flux calibration over the full wavelength range using the different standard stars, and significantly less variation over the wavelength width of the flux peaks that we measure in Section 6.2.

The FIRE spectrum was extracted using the low-dispersion version of the FIREHOSE pipeline, which is based on the MASE pipeline (Bochanski et al. 2009; Simcoe et al. 2010). The pipeline uses a flat-field constructed from two quartz lamp images taken with the lamp at high (2.5 V) and low (1.5 V) voltage settings. The data were divided by this pixel flat before being wavelength calibrated. The pipeline performs sky subtraction following the method outlined in Bochanski et al. (2011), adapted for the low-dispersion configuration of the spectrograph. The spectra were optimally extracted before being combined using a weighted mean, using an adaptation of the XCOMBSPEC routine from SPEXTOOL (Cushing, Vacca & Rayner 2004). The T dwarf spectra were then corrected for tel-

luric absorption and flux calibrated using a FIRE specific version of the XTELLCOR routine (Vacca, Cushing & Rayner 2003). Finally, residual outlying points due to cosmic rays and bad pixels were removed using a simple 3σ clipping algorithm.

6 OBJECTS OF SPECIAL NOTE

6.1 WISE 1639–6847

The brightest (in *W2*) source in our sample is WISE 1639–6847, which we analysed while assessing sample candidates. This object was recently presented by Tinney et al. (2012), who used differential imaging to separate the *J*-band counterpart from a nearby blended star ~ 6 arcsec to the south of the object (measuring a colour of $J_3 - W2 = 6.98$). These authors also measured the object's spectrum during a period of good (~ 0.6 arcsec) seeing, and determined a spectral type of Y0. They also combined the *WISE* All-Sky and 3-Band Cryo images with their *J*-band data to measure proper motion and parallax constraints, determining a proper motion of 3.07 ± 0.04 arcsec yr⁻¹ and an approximate distance of ~ 5 pc. We did not measure the near-infrared counterpart, but we used the *WISE* data by itself to assess source motion and determine proper motion constraints. It is interesting to compare our results to those obtained with more data.

Examination of the blended source in 2MASS, SuperCOSMOS and *W1* revealed that it was a non-moving point source with $\sim K$ -star colours. To remove the blended source from the *W2* image we used PSF subtraction. We identified an isolated PSF-subtraction source ~ 30 arcsec south-west of the blended source, extracted a sky-subtracted *W2* image region centred on PSF-subtraction source (and absent of any other sources), normalized this to account for the *W2* flux difference between the blended source and the PSF-subtraction source, and made a spatial shift to the blended star *WISE* position (which is well measured from the *W1* image). This

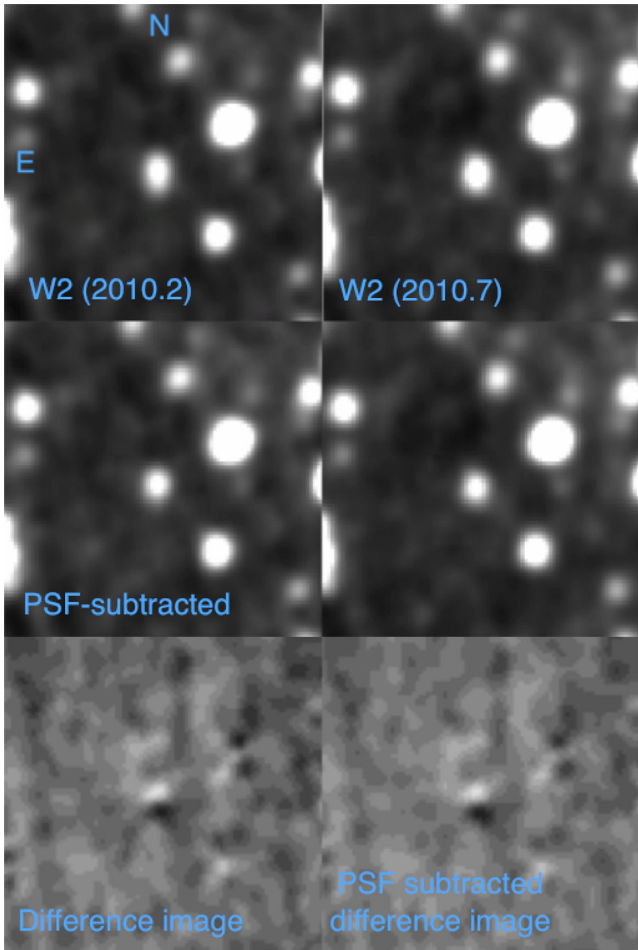


Figure 4. W2 images of WISE 1639–6847. The top two images show the *WISE* All-Sky and 3-Band Cryo images on the left and right, respectively, which are separated in epoch by ~ 6 months. The PSF of the non-moving blend star has been subtracted in the middle two images, with WISE 1639–6847 now seen to be a point source that moves ~ 1 pixel southwards between these epochs. This motion is also shown by the difference images in the bottom two plots (see the text).

normalized shifted PSF-subtraction source was then subtracted off the W2 image to effectively remove the PSF of the blended source.

In Fig. 4, the top-left and right W2 images are from the *WISE*-All-Sky and 3-Band Cryo releases, respectively (~ 6 months apart). The middle two plots show our blend-subtracted images where WISE 1639–6847 now appears as a circular point-like source. The proper motion was measured using these blend-subtracted images. We used the *IRAF*, *GEOMAP* and *GEOXYTRAN* packages to derive positional transforms between the two epoch images. As reference stars we selected sources that had good signal-to-noise (> 20), were unsaturated and point-like in both epoch images, and were within 5 arcmin of the candidate. We selected 20 reference stars, optimized a fit geometry of second-order polynomials in x and y , and rejected outlier reference stars. The root-mean-square residuals of our fitted transform were 0.05 pixels (~ 70 mas). To estimate centroiding uncertainties for *WISE* sources, we used the astrometric relation described in Wright et al. (2010) with a correction factor of $\text{FWHM}_{W2}/\text{FWHM}_{W1}$ since our sources are W2-only ($\sigma = 0.18 + 6.4/(2\text{SNR})$). In this way, we determined proper motion constraints for WISE 1639–6847 of $\mu_{\alpha} = -0.8 \pm 1.2$ arcsec yr $^{-1}$ and $\mu_{\delta} = 2.8 \pm 1.2$ arcsec yr $^{-1}$. These have much larger uncertain-

ties than the Tinney et al. results but are consistent, and significant at the level of $\sim 2.5\sigma$.

We also studied the signature of motion in the *WISE* data by assessing the difference image (epoch 1 minus epoch 2) which is shown at the bottom of Fig. 4. The left-hand image shows the difference between the original *WISE* epoch images while the other image was made using the blend-subtracted versions. These two images are very similar as expected, since the subtraction of the stationary blend star should not significantly affect the difference image. The motion of the source between the epochs results in a positive–negative undulation following the direction of motion. We note other features in the difference images associated with bright sources, whose profiles are not stable between the epochs, and also some that result from faint non-point-like features. However, the difference signature of WISE 1639–6847 is clear, and it seems likely that the depth and symmetry properties of such difference image undulations could be combined with source brightness information to provide a general means of assessing the credence of moving object candidates in *WISE* multi-epoch data.

6.2 WISE 0013+0634 and WISE 0833+0052

Fig. 5 shows images of WISE 0013+0634 in various bands. The W2 and W1 *WISE* images are shown upper-left and -right respectively (epoch 2010.5), with two epochs of *J*-band imaging below with the near-infrared counterpart indicated by a red arrow. The bottom-right zoomed in image shows a low signal-to-noise (~ 5) counterpart from the UKIDSS LAS (epoch 2008.9). This counterpart is offset by ~ 2 arcsec from the *WISE* source centre, and no detections were discernible in the *Y*-, *H*- or *K*-band LAS images. We were able to confirm the near-infrared counterpart in a deeper *J*-band image (using Four Star on Magellan; epoch 2012.6) in which we detected the counterpart with signal-to-noise ~ 20 on the other side of the

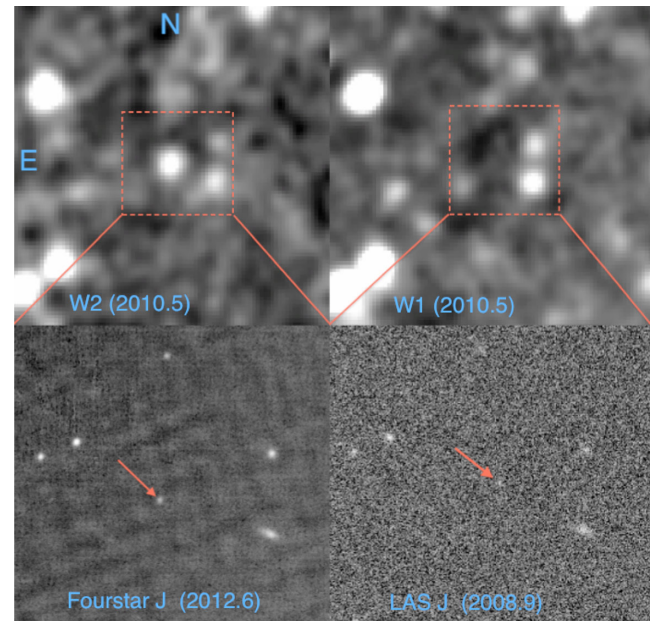


Figure 5. Multiband images of WISE 0013+0634. The top two plots are *WISE* W2- and W1-band images on the left and right, respectively, with the source in the centre. The bottom two plots show the Magellan Four Star and UKIDSS LAS *J*-band zoomed in images on the left and right, respectively. The epoch difference between these two images is 3.7 yr. The high proper motion *J*-band counterpart is indicated in each image by a red arrow.

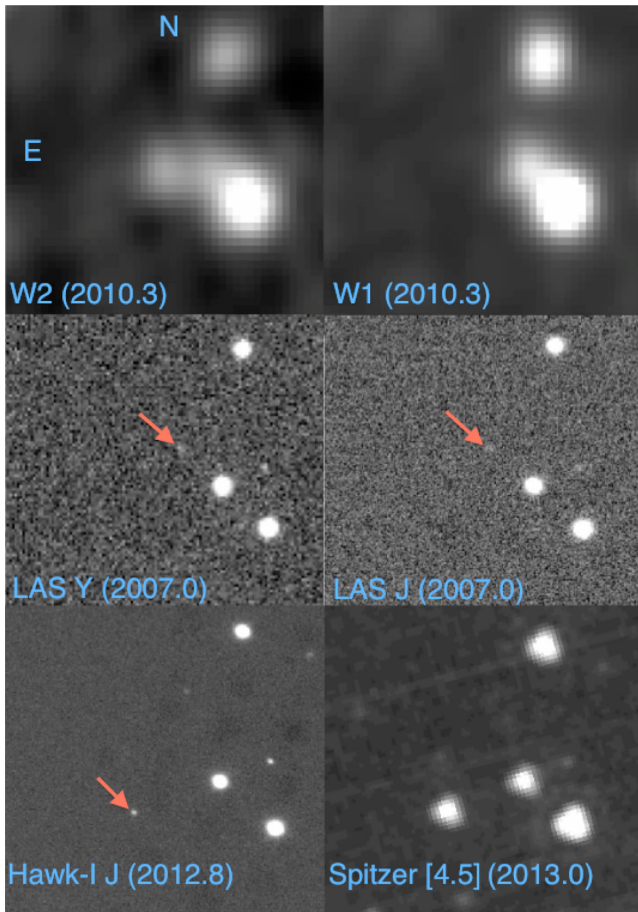


Figure 6. Multiband images of WISE 0833+0052. Each image is 1 arcmin on the side. The top two plots are *WISE* W2- and W1-band images on the left and right, respectively, with WISE 0833+0052 in the centre. The middle two plots show the UKIDSS Y- and J-band images from 2006.95. The bottom two plots show the VLT Hawk-I J image from 2012.8 and the *Spitzer* [4.5] image from 2013.0. The high proper motion near-infrared counterpart is indicated in each image by a red arrow, and has moved by 10.4 arcsec across the near-infrared epochs.

WISE source centre. The three epoch positions (UKIDSS, *WISE* and Magellan) are all consistent with our measured proper motion (to within astrometric uncertainties), though our final proper motion of $1.3 \text{ arcsec yr}^{-1}$ was derived using the UKIDSS and Magellan data (with a 3.7 yr baseline).

WISE 0833+0052 is the brightest ($W2 = 14.96$) new object in our sample. Fig. 6 shows the *WISE* images at the top (epoch 2010.32) with the *WISE* counterpart slightly blended with a star ~ 10 arcsec to the west. The middle two plots show the UKIDSS LAS Y- and J-band images from 2007.0 (the counterpart was undetected in the LAS H- and K-band images), and the bottom two plots show the J-band Hawk-I image from 2012.8 and the *Spitzer* [4.5] image from 2013.0. A faint UKIDSS Y- and J-band counterpart is visible at low signal-to-noise about 6 arcsec to the north-west of the *WISE* source centre. And in the more recent VLT and *Spitzer* epochs, the source is strongly detected about 4 arcsec to the south-east of the *WISE* position. We measured the proper motion of WISE 0833+0052 using the UKIDSS and HAWK-I J-band images. We also verified that the positions in UKIDSS, *WISE* and *Spitzer* were consistent with this. Our centroiding on the *WISE* source was not affected by the modest level of blending evident in the W2 image, so our

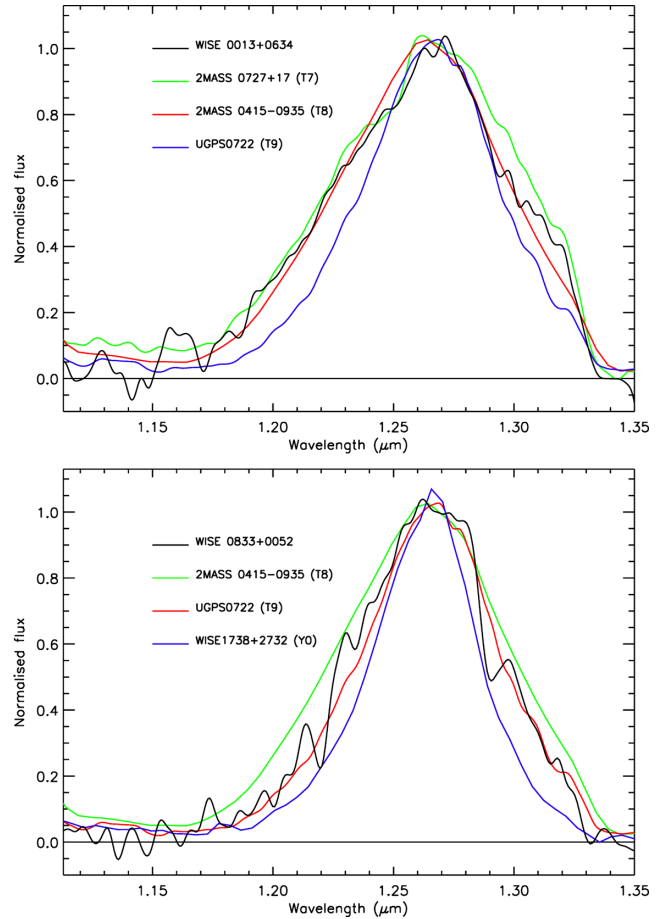


Figure 7. The J-band spectra of WISE 0013+0634 and WISE 0833+0052. Late-T standard spectra are overplotted for comparison and to facilitate spectral typing.

consistency check was able to verify the relative location of the object in all the epochs. WISE 0833+0052 has a high proper motion of $1.89 \pm 0.04 \text{ arcsec yr}^{-1}$.

Fig. 7 shows the J-band spectra of WISE 0013+0634 and WISE 0833+0052. In the top plot, we compare to the spectra of three normal T dwarfs with known spectral types; T7 (2MASS 0727+1710), T8 (2MASS 0415-0935) and T9 (UGPS 0722-0540). Similarly, in the bottom plot, we compare with WISE J1738+2732 (Y0) in addition to the T8 and T9 examples. All spectra have been normalized to an average of unity in the 1.265–1.275 μm spectral range. The J-band flux peak is sculpted by strong CH_4 and H_2O absorption, and its width is a well-established diagnostic for low T_{eff} amongst late-L, T and early-Y dwarfs (e.g. Burgasser et al 2006; Burningham et al. 2008; K12). We focus on the J-band peaks for spectral typing since this region provides the best signal-to-noise in our spectra. In the top plot, it can be seen that the J-band flux peak of WISE 0013+0634 is most similar to the T8 comparison. The J-band flux peak of the T9 comparison has a significantly steeper blue wing, and the red wing of the T7 comparison flux peak is significantly brighter in the 1.28–1.32 μm range. We thus assign a spectral type of $T8 \pm 0.5$ to WISE 0013+0634. In the bottom plot, the J-band flux peak of WISE 0833+0052 has a very similar width and shape to that of UGPS 0722-0540, and is clearly intermediate between (and significantly different to) the T8 and Y0 comparison spectra. We thus assign a spectral type of $T9 \pm 0.5$ to WISE 0833+0052.

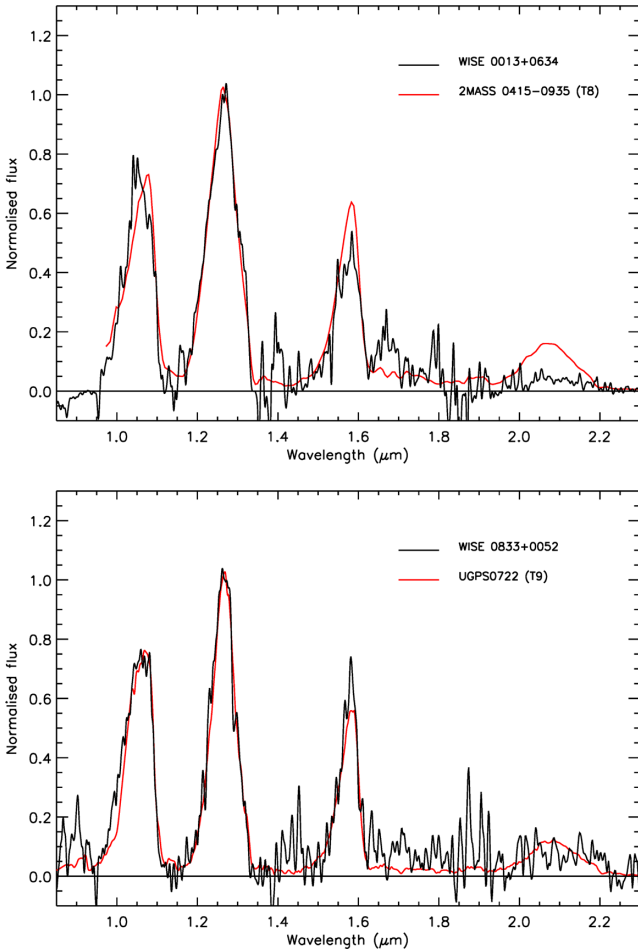


Figure 8. The full near-infrared spectrum of WISE 0013+0634 and WISE 0833+0052. A known T8 and T9 dwarf are overplotted in red for comparison.

To compare the overall spectral morphology and colours of WISE 0013+0634 and WISE 0833+0052 with those of other field objects, we show their full near-infrared spectra and measured colours in Figs 8 and 9. When plotting the spectra we also show (in red) comparison T8 and T9 spectra for WISE 0013+0634 and WISE 0833+0052, respectively. In the colour plots, WISE 0013+0634 and WISE 0833+0052 are represented by red symbols, with a comparison sample of late-T and Y dwarfs from Leggett et al. (2013) plotted in blue.

We note that the Y -band flux peak of WISE 0833+0052 is not markedly different from that of UGPS 0722–0540, which seems surprising since the measured $Y - J$ colour of WISE 0833+0052 is bluer than all the late-T dwarfs in Fig. 9. While the Y -band peak of WISE 0833+0052 is slightly broader (extending to the blue), this can only account for a small ~ 7 per cent Y -band excess (relative to J), which is insufficient to explain the measured $Y - J$ colour. However, the Y -band photometric uncertainties are large due to low signal-to-noise (± 0.2), and the measured $Y - J$ colour is only $\sim 2\sigma$ away from a more typical value for late-T dwarfs. So while this potential anomaly may offer tentative evidence of variability, further photometric studies (at higher signal-to-noise) will be needed to investigate this possibility.

WISE 0013+0634 is significantly K band suppressed by comparison with 2MASS 0415–0935, and despite a rather noisier K -band spectrum WISE 0833+0052 appears to be K band suppressed also.

Theory and observation suggest this is due to strong collisionally induced absorption by H_2 in higher pressure atmospheres with low-metallicity and/or high-gravity (e.g. Saumon et al. 1994; Pinfield et al. 2008).

The H -band flux peak of WISE 0013+0634 appears slightly suppressed relative to 2MASS 0415–0935, and that of WISE 0833+0052 seems slightly enhanced compared to UGPS 0722–0540. However, there is no evidence that they are outliers in $J - H$ colour, and we note that the broad-band spectroscopic flux calibration for WISE 0833+0052 is no better than ~ 10 per cent.

The range of plots shown in Fig. 9 clearly demonstrate that WISE 0013+0634 and WISE 0833+0052 have relatively enhanced mid-infrared emission compared to their near-infrared brightness. This excess is seen in the $H - W_2$ versus spectral type plot, where both objects lie significantly above the locus of other T dwarfs (~ 1 – 1.5 mag redder than the average T dwarf colour). However, in $J - H$ and mid-infrared colours they do not appear unusual. The only comparison object with a similar excess is the T7.5p dwarf ULAS 1416+13B, which is believed to be a low-metallicity/high-gravity object (Burningham et al. 2010a). Theory (Saumon & Marley 2008; Allard, Homeier & Freytag 2011) predicts a change in $H - W_2$ of $+0.2$ to $+0.3$ for a decrease in metallicity of $\Delta[M/H] = -0.3$ (at $T_{\text{eff}} \sim 700$ K), while studies of metal poor benchmarks (e.g. Pinfield et al. 2012) suggest even larger effects ($\Delta H - W_2 = +0.6$; Burningham et al. 2013). Overall, current theory and observation would suggest that $\Delta H - W_2 = 1$ – 1.5 could suggest a low-metallicity object with $[M/H]$ between -0.5 and -1.5 .

We have estimated the distances of WISE 0013+0634 and WISE 0833+0052 using absolute magnitude against spectral type relations from Dupuy & Liu (2012), in all available bands (and allowing for a spectral type uncertainty of ± 0.5 types). The results are shown in Table 7 for both the single object case and that of an unresolved binary with equal brightness components. For both objects, these distance constraints fall into two groupings. Distance estimates made in the J and H bands are the largest, with those made in the mid-infrared (and the Y band for WISE 0833+0052) being smaller by a factor of ~ 2 . As previously discussed, the Y -band magnitude has large uncertainty, but the factor of ~ 2 difference between the JH and mid-infrared distance estimates is clear, and in itself is representative of an ~ 1.5 magnitude relative mid-infrared/ JH excess (compared to typical T8–9 field dwarfs). The actual distances of WISE 0013+0634 and WISE 0833+0052 may be intermediate between the near- and mid-infrared estimates, and will be greater if the object is an unresolved multiple.

We now use our distance estimates to place constraints on the space motions of WISE 0013+0634 and WISE 0833+0052. We use the single object distances to avoid overestimating space motion, and we combine together our distance estimates into a JH constraint (D_{JH}) and a mid-infrared constraint (D_{MIR}). WISE 0013+0634 thus has $D_{JH} = 36$ – 55 pc and $D_{\text{MIR}} = 18$ – 30 pc, while WISE 0833+0052 has $D_{JH} = 27$ – 37 pc and $D_{\text{MIR}} = 15$ – 19 pc. We have used these distance estimates to construct the space motion diagrams shown in Fig. 10. The velocity components U , V and W are directed to the Galactic anticentre, rotation direction and north Galactic pole, respectively, and have been corrected for the local solar motion (U_{\odot} , V_{\odot} , W_{\odot}) = $(-8.5, 13.38, 6.49)$ km s $^{-1}$ with respect to the local standard of rest (Coşkunoğlu et al. 2011). WISE 0013+0634 is shown in the top plots, with WISE 0833+0052 in the bottom plots. The left-hand plots were constructed using the JH distances, while the right-hand plots use the closer mid-infrared estimates. We also allow for proper motion uncertainties (which are of relatively minor importance) and possible radial velocity (RV) in the range -250

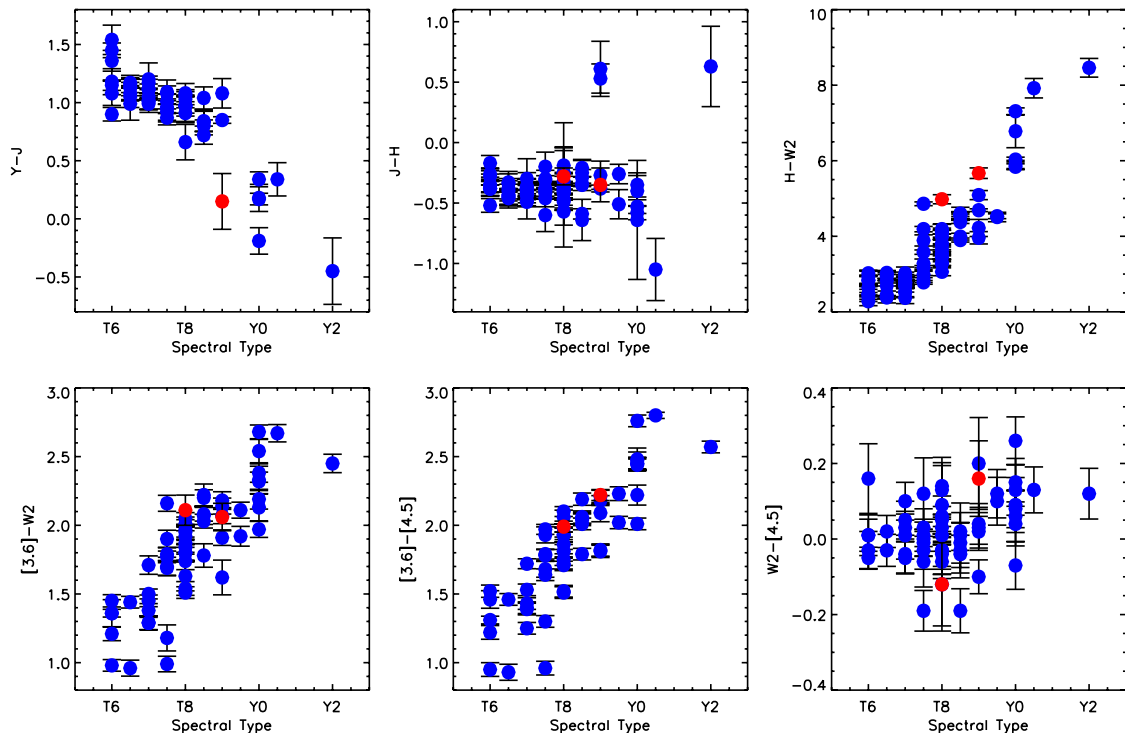


Figure 9. Plots of various colours as a function of spectral type. WISE 0013+0634 (T8) and WISE 0833+0052 (T9) are red, and the comparison sample of late-T and Y dwarfs from Leggett et al. (2013) is in blue.

Table 7. Distance estimates for WISE 0013+0634 and WISE 0833+0052 using absolute magnitude versus spectral type relations in the Y , J , H , [3.6], [4.5] and $W2$ bands (where available), and spectral types of $T8 \pm 0.5$ and $T9 \pm 0.5$, respectively. Absolute magnitudes have been estimated assuming single objects and also equal brightness unresolved binarity.

WISE 0013+0634 ($T8 \pm 0.5$)		Distance range (pc)	
Band	Single object	Unresolved binary	
J	46 (39–55)	65 (55–78)	
H	43 (36–51)	61 (51–73)	
[3.6]	26 (23–30)	37 (33–42)	
[4.5]	22 (20–25)	31 (28–35)	
$W2$	21 (18–25)	30 (25–35)	
WISE 0833+0052 ($T9 \pm 0.5$)		Distance range (pc)	
Band	Single object	Unresolved binary	
Y	22 (18–26)	31 (26–37)	
J	31 (26–37)	44 (37–52)	
H	32 (27–38)	45 (37–53)	
[3.6]	17 (15–19)	24 (21–27)	
[4.5]	15 (14–17)	22 (20–24)	
$W2$	17 (15–20)	24 (21–29)	

to $+250 \text{ km s}^{-1}$ when calculating space motions, with the resulting constraints being shown as grey regions in the plots. As a guide we overplot the mid-value space motion in red, with blue and green symbols indicating how the uncertainty in distance and RV broadens the constrained region. We also overplot the old disc and halo veloc-

ity dispersions (1 and 2σ as dashed/dotted and solid lines, respectively) from Chiba & Beers (2000). In Table 8, we present tangential velocity estimates for WISE 0013+0634 and WISE 0833+0052 (with ranges reflecting proper motion and distance uncertainties), as well as minimum possible value estimates for total space motion ($\sqrt{(U^2 + V^2 + W^2)}_{\min}$ in the LSR frame). These minimum space motions result from a UVW parameter-space search (i.e. within the grey regions in Fig. 10) for each object. The solar-centric RV that would produce the minimum space motions are indicated in parentheses in the table, with all other RV values leading to larger space motions.

It is clear that when the JH distances are used, WISE 0013+0634 and WISE 0833+0052 occupy the halo region in Fig. 10. This is also evident in Table 8, where the minimum possible space motions (if we assume D_{JH}) are above the range defined for the thick disc ($85\text{--}180 \text{ km s}^{-1}$; Fuhrmann 2000; Feltzing, Bensby & Lundström 2003; Nissen 2004). However, if we instead use the mid-infrared distance estimates the space motions could be lower, touching or overlapping with the 2σ old disc velocity dispersion in Fig. 10. In this case, the total space motion would also be consistent with thick disc membership.

The actual distances of WISE 0013+0634 and WISE 0833+0052 may be intermediate between D_{JH} and D_{MIR} (e.g. consider the measured absolute magnitudes of the low-metallicity/high-gravity dwarf ULAS 1416+13B; Dupuy & Liu 2012), with space motions that are similarly intermediate. Taking an average (of the D_{JH} and D_{MIR} cases) minimum space motion for WISE 0013+0634 gives 133 km s^{-1} , while for WISE 0833+0052 the average is 170 km s^{-1} . Parallax distance and RB will be crucial measurements for both these objects to properly establish their space motions, but it seems likely even at this stage that WISE 0833+0052 could have unambiguous halo kinematics.

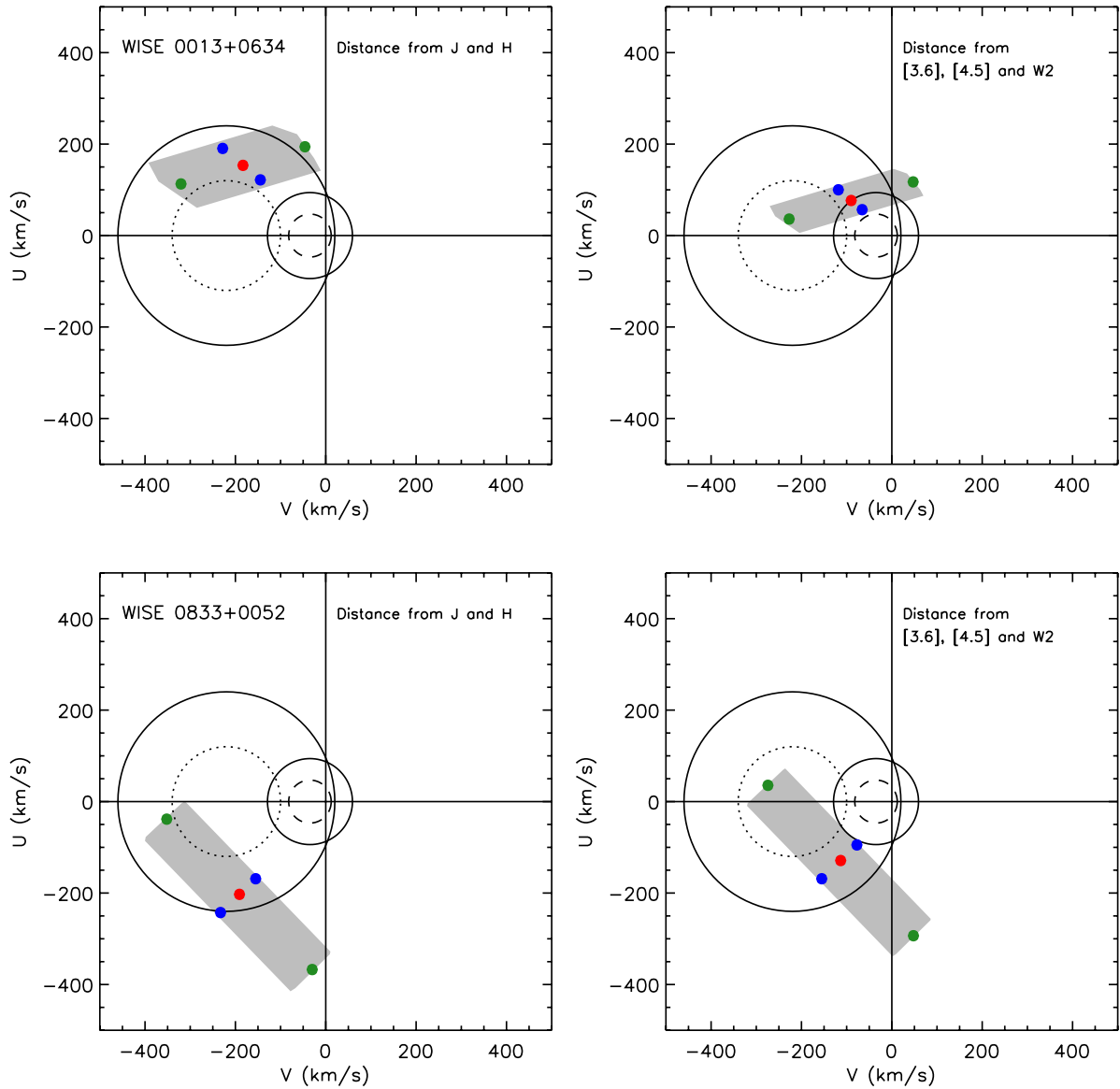


Figure 10. UV space motion plots for WISE 0013+0634 and WISE 0833+0052. Uncertainties in measured proper motion and estimated distance have been accounted for, as well as a possible range in RV from -250 to $+250$ km s^{-1} . In the left-hand plots distances were estimated using JH brightness, while in the right-hand plots they were estimated using (relatively overluminous) mid-infrared brightness. Old disc and halo velocity dispersions (1 and 2σ as dashed/dotted and solid lines, respectively) are also shown from Chiba & Beers (2000).

Table 8. Tangential velocities and minimum values of the total space motion ($\sqrt{(U^2 + V^2 + W^2)}_{\min}$) for WISE 0013+0634 and WISE 0833+0052. The solar-centric radial velocity (RV in km s^{-1}) required to produce the minimum space motion is also listed.

Object	V_{tan} (km s^{-1})		Minimum space motion (km s^{-1}) $= \sqrt{(U^2 + V^2 + W^2)}_{\min}$	
	Using D_{JH}	Using D_{MIR}	Using D_{JH}	Using D_{MIR}
WISE 0013+0634	278 (213–349)	147 (107–190)	183 (RV = -1)	83 (RV = -1)
WISE 0833+0052	286 (235–337)	179 (126–231)	222 (RV = 12)	118 (RV = 12)

7 REDUCED PROPER MOTION DIAGRAM

In Fig. 11, we plot reduced proper motion ($H_{W2} = W2 + 5 \log \mu + 5$) against $W1 - W2$ and spectral type (left- and right-hand plots, respectively). In the top two plots, WISE 0013+0634 and WISE 0833+0052 are shown as red symbols. We also plot (as blue sym-

bols) a sample that includes the *WISE* census (with proper motions from K11) and all additional L and T dwarfs from DwarfArchives (if they are detected in *WISE* and have proper motion accuracy ≤ 25 per cent). L sub-dwarfs are shown as open symbols in the top plots, and Y dwarfs as green. Y dwarfs with parallax measurements are individually labelled in the left-hand plot. We also overplot

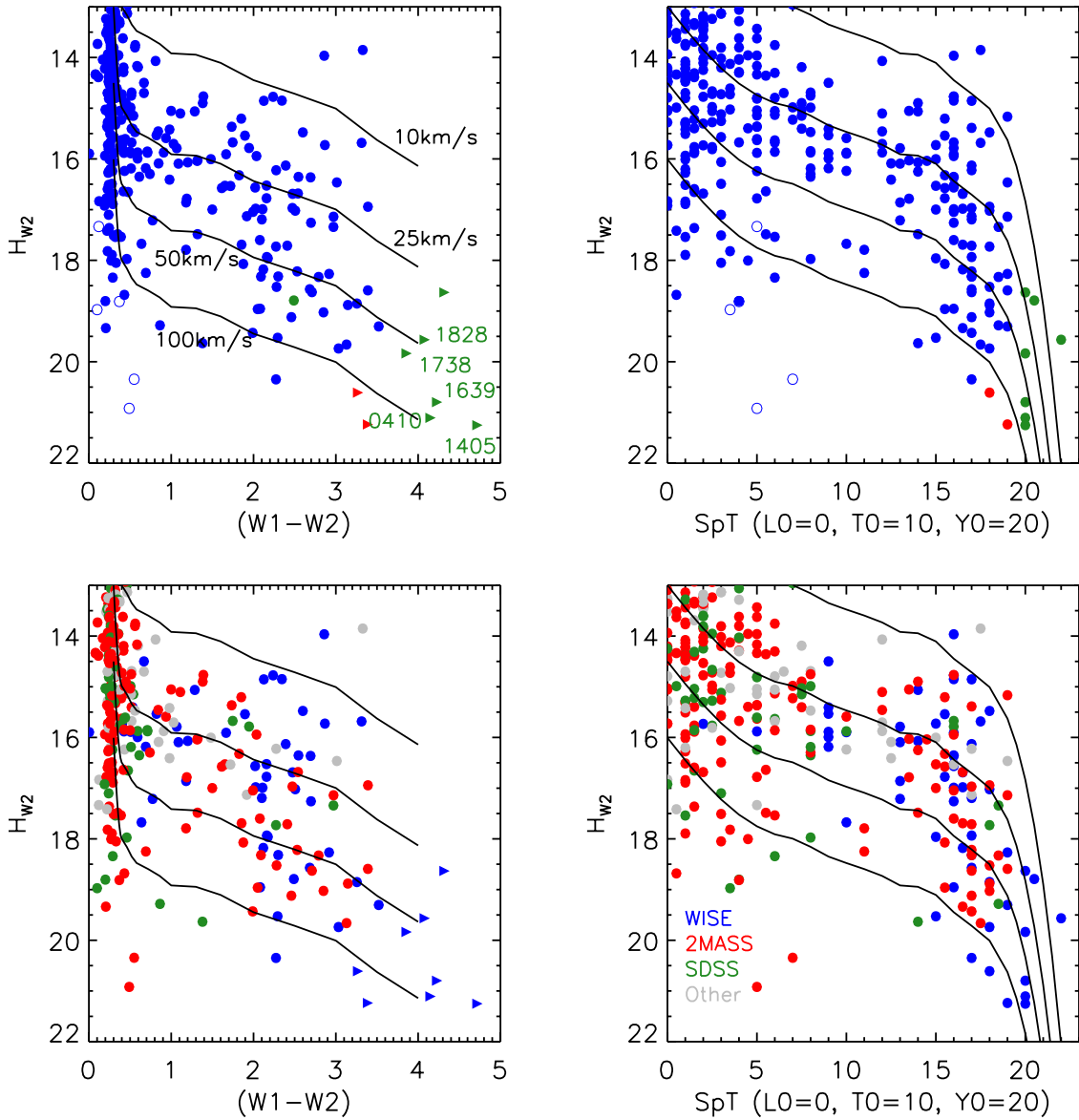


Figure 11. Diagrams showing reduced proper motion against colour (left) and spectral type (right). In the top two plots, the DwarfArchive and K12 census are plotted in blue using proper motions from K11. Y dwarfs are green and ultracool sub-dwarfs as open symbols. WISE 0013+0634 and WISE 0833+0052 are red. In the bottom two plots, the colour coding shows the survey used to identify each object (*WISE*, 2MASS, SDSS and others).

indicative tracks to show characteristic kinematics, for L0-T9.5 and L0-Y2 dwarfs in the left- and right-hand plots, respectively. These tracks were constructed using the K12 M_{W2} relationship (the fit excluding WISE 1828+2650) for T7-Y2 dwarfs, combined with estimates of M_{W2} for the L0-T6.5 dwarfs (which were derived using an $H - W2$ colour-corrected M_H relation from Marocco et al. (2010)). For the left-hand plot, we made use of a $W1 - W2$ colour-spectral type relationship constructed using data from K12.

In the bottom two plots, we show the same objects but with different colours representing the surveys in which they were identified. The *WISE* census is shown in blue, 2MASS in red and SDSS in green. Other objects (grey) mainly come from DENIS, with the UKIDSS and CFBDS surveys only yielding nine and one object, respectively (that were detected in *WISE* and with <25 per cent proper motion uncertainties).

The left-hand plots suffer from a bunching-up of the tracks for blue objects due to the relative insensitivity of the $W1 - W2$ colour

to types earlier than \sim mid-L. However, the right-hand plots shows a similar effect for the latest objects, as the M_{W2} plummets in the Y dwarf regime. For the bluest colours (around L0), there is a full spread across the $V_{\text{tan}} = 10\text{--}100 \text{ km s}^{-1}$ range. This is the most populated part of the diagram. Moving to redder, later types the diagram becomes more sparsely populated, and it is clear that L-mid T dwarfs ($W1 - W2 < 2$) with $V_{\text{tan}} = 50\text{--}100 \text{ km s}^{-1}$ are rare compared to those with $V_{\text{tan}} = 10\text{--}50 \text{ km s}^{-1}$. This is consistent with previous kinematic studies of ultracool dwarfs across the M7-T range (e.g. fig. 7 of Faherty et al. 2009) that show a V_{tan} distribution peaking at $10\text{--}30 \text{ km s}^{-1}$, with ~ 85 per cent having $V_{\text{tan}} < 50 \text{ km s}^{-1}$ and relatively very few with $V_{\text{tan}} \sim 100 \text{ km s}^{-1}$ or more. However, for mid-T and later ($W1 - W2 > 2$) there appears to be a significantly larger scatter in V_{tan} , with WISE 0013+0634 and WISE 0833+0052 establishing the extremes of reduced proper motion for the latest T dwarfs. This may suggest that the fraction of field brown dwarfs with thick-disc/halo kinematics is greater for mid-late T dwarfs than

for earlier objects. Indeed, the start of this trend may be evident in fig. 6 of Faherty et al. (2009).

The situation is slightly more ambiguous for the Y dwarfs, since the tracks only extend out to T9.5 colours in the left-hand plot, and in the right-hand plot they steepen rapidly into the Y dwarf regime. However, parallax distance estimates are available for five of the Y dwarfs in the diagram, and are suggestive. WISE 1828+2650 and WISE 1738+2732 have V_{tan} in the range 25–95 km s⁻¹, while WISE 0410+1502 and WISE 1405+5534 have $V_{\text{tan}} > 100$ km s⁻¹, and WISE 1639–6847 has $V_{\text{tan}} = 73 \pm 8$ km s⁻¹ (see also Tinney et al. 2012).

The bottom two plots show that the larger scatter in mid–late T reduced proper motion is evident amongst the samples from both *WISE* and 2MASS, though there are insufficient SDSS objects plotted to assess this survey sample. We considered possible selection biases for these survey samples that might contribute to the scatter. Leggett et al. (2010) examines the mid-infrared properties of late-T dwarfs, and highlights the T6–6.5 dwarfs 2MASS 0937+2931 and 2MASS 1237+6526. These T dwarfs ($T_{\text{eff}} = 800\text{--}975\text{K}$) are believed to be metal poor ($[M/H] \simeq -0.3$ and -0.2 , respectively) from spectroscopic fitting (Liebert & Burgasser 2007; Geballe et al. 2009), and show $M_{[4.5]}$ excess (at a level of ~ 0.5 mag) with respect to the solar/rich metallicity T7.5 dwarfs Gl 570D and HD 3651B ($T_{\text{eff}} = 780\text{--}840\text{K}$). If metal-poor mid–late T dwarfs can be detected out to distances ≥ 25 per cent further than their solar/rich analogues, we might expect a factor ≥ 2 increase in their number in a *W2*-limited *WISE* sample. Metal poor T dwarfs could constitute a kinematically older population with larger velocity dispersion. Also standard 2MASS T dwarf selection techniques require blue $H - K$ colours which will introduce a bias towards older lower metallicity objects, which could affect their kinematics in a similar sense. To address these possible biases it would be interesting to compare the reduced proper motions of a large sample of mid–late T dwarfs from the UKIDSS and VISTA surveys (e.g. building on Lodieu et al. 2012b; Burningham et al. 2013), since those selection techniques should not lead to an older metal poor bias. And for the Y dwarfs, the kinematic constraints are determined by parallax distances that need to be improved.

If the large scatter in reduced proper motion for late-T and Y dwarfs genuinely results from an increased fraction of objects with $V_{\text{tan}} = 50\text{--}100$ km s⁻¹, this may provide useful constraints on the mass function and evolution of brown dwarfs. A 10 Gyr-old early- to mid-T dwarf with $T_{\text{eff}} = 1000\text{--}1400\text{K}$ will have a mass of about 70–80 M_{Jupiter} , while a 10 Gyr-old late-T to early-Y dwarf with $T_{\text{eff}} = 400\text{--}800\text{K}$ will have a mass of 25–65 M_{Jupiter} (Burrows et al. 2001). For a flat or slightly declining mass function, we would therefore expect to see more late-T/Y than early–mid T thick disc brown dwarfs.

8 SUMMARY AND FUTURE WORK

We have presented a new method for identifying late-T and Y dwarf candidates in the *WISE* data base. After an initial selection of sources with at least eight individual frames measured per band, detections in *W2*-only were selected avoiding directions where extinction $A_v > 0.8$. We then developed rejection methods to assess the nature of the *W2* sources, using the information relating to the multiple measurements and the source profile-fitting. These methods were designed to reject non-point-like, variable and moving (Solar system) objects, and were based on measures of the profile fit photometry, the scatter in the individual *W2* measurements, and the fraction of individual detections in the full *W2*

frame set. To effectively trace the desired parameter-space, we made use of a control sample of isolated non-moving non-variable point sources from the SDSS. These methods led to a manageable sample size for visual inspection down to $w2\text{snr} = 10$, and with the additional removal of sources near bright 2MASS stars, down to $w2\text{snr} = 8$.

We identify 158 candidate late objects. For $w2\text{snr} > 10 \sim 45$ per cent are not identified by the previously published method of K12, and for the lower $w2\text{snr} = 8\text{--}10$ sources ~ 90 per cent fall outside the K12 criteria. The main reason for this is the differing approaches used to place constraints on the number of individual *W2* detections. The main source of incompleteness in our sample is source blending, which can affect the statistical properties that we assess, although we do not directly reject blends in our search method.

Our analysis of WISE 1639–6847 shows that the ~ 6 month baseline offered by the full *WISE* data set can yield reasonably accurate proper motions for high proper motion objects, and that difference images may be a useful tool.

We have identified two high proper motion late-T dwarfs, a T8 WISE 0013+0634 and a T9 WISE 0833+0052. These objects both show mid-infrared/near-infrared excess and *K*-band suppression consistent with high gravity and/or low metallicity. Distance estimates lead to kinematics that are consistent with thick disc or halo membership, and current constraints suggest that WISE 0833+0052 may have unambiguous halo kinematics.

Examination of reduced proper motion diagrams suggests that late-T and Y dwarfs may consist of a larger fraction of thick-disc/halo members than is the case for earlier objects.

Parallax and RV measurements for WISE 0013+0634 and WISE 0833+0052 are vital to properly determine the space motion of these objects. And additional near-infrared follow-up will allow us to categorise candidates in our full sample (according to Table 3), and build up the known number of very late T and Y dwarfs across the range of kinematic populations.

ACKNOWLEDGEMENTS

This publication makes use of data products from the Wide-field Infrared Survey Explorer, which is a joint project of the University of California, Los Angeles, and the Jet Propulsion Laboratory/California Institute of Technology, funded by the National Aeronautics and Space Administration. The UKIDSS project is defined in Lawrence et al. (2007). UKIDSS uses the UKIRT WFCAM (Casali et al. 2007) and a photometric system described in Hewett et al. (2006). The CASU pipeline processing and science archive are described in Irwin et al. (2004) and Hambly et al. (2008). Based on observations obtained as part of the VISTA Hemisphere Survey, ESO Programme 179.A-2010 (PI: McMahon). This paper includes data gathered with the 6.5 metre Magellan Telescopes located at Las Campanas Observatory, Chile (programme number CN2012B-019). Based on observations made with the Italian Telescopio Nazionale Galileo (AOT26TAC68/AOT22TAC96) operated on the island of La Palma by the Fundación Galileo Galilei of the INAF (Istituto Nazionale di Astrofisica) at the Spanish Observatorio del Roque de los Muchachos of the Instituto de Astrofísica de Canarias. Observations have been made using the SofI instrument on ESO's New Technology Telescope as part of programme 090.C-0791(A). DP, NL, MG and HJ have received support from RoPACS during this research, and JG, ADJ and JJ have been supported by RoPACS, a Marie Curie Initial Training Network funded by the European Commissions Seventh Framework Programme.

ADJ is supported by a Fondecyt Postdoctorado under project number 3100098. SKL is supported by the Gemini Observatory, which is operated by AURA, on behalf of the international Gemini partnership of Argentina, Australia, Brazil, Canada, Chile, the United Kingdom and the United States of America. MG is financed by the GEMINI-CONICYT Fund, allocated to the project 32110014. MTR is partially funded by PB06, CATA. RK acknowledges partial support from FONDECYT through grant number 1130140. NL is funded by the national program AYA2010-19136 funded by the Spanish ministry of science and innovation. VJSB has been supported by the Spanish Ministry of Economics and Competitiveness under the project AYA2010-20535. This research has made use of the SIMBAD data base, operated at CDS, Strasbourg, France. This research has benefited from the SpeX Prism Spectral Libraries, maintained by Adam Burgasser at <http://pono.ucsd.edu/~adam/browndwarfs/speXprism>.

REFERENCES

- Allard F., Homeier D., Freytag B., 2011, in Johns-Krull C., Browning M. K., West A. A., eds, ASP Conf. Ser. Vol. 448, Model Atmospheres From Very Low Mass Stars to Brown Dwarfs. Astron. Soc. Pac., San Francisco, p. 91
- Allard F., Homeier D., Freytag B., 2012, *Phil. Trans. R. Soc. A*, 370, 2765
- Baffa C. et al., 2001, *A&A*, 378, 722
- Baraffe I., Chabrier G., Barman T. S., Allard F., Hauschildt P. H., 2003, *A&A*, 402, 701
- Bastian N., Covey K. R., Meyer M. R., 2010, *ARA&A*, 48, 339
- Bate M. R., Bonnell I. A., Bromm V., 2002, *MNRAS*, 332, L65
- Bochanski J. J. et al., 2009, *PASP*, 121, 1409
- Bochanski J. J., Burgasser A. J., Simcoe R. A., West A. A., 2011, *AJ*, 142, 169
- Bonnell I. A., Clark P., Bate M. R., 2008, *MNRAS*, 389, 1556
- Burgasser A. J., Geballe T. R., Leggett S. K., Kirkpatrick J. D., Golimowski D. A., 2006, *ApJ*, 637, 1067
- Burningham B. et al., 2008, *MNRAS*, 391, 320
- Burningham B. et al., 2009, *MNRAS*, 395, 1237
- Burningham B. et al., 2010a, *MNRAS*, 404, 1952
- Burningham B. et al., 2010b, *MNRAS*, 406, 1885
- Burningham B. et al., 2013, *MNRAS*, 433, 457
- Burrows A., Hubbard W. B., Lunine J. I., Liebert J., 2001, *Rev. Mod. Phys.*, 73, 719
- Burrows A., Sudarsky D., Lunine J. I., 2003, *ApJ*, 596, 587
- Carpenter J. M., 2001, *AJ*, 121, 2851
- Casali M. et al., 2007, *A&A*, 467, 777
- Castro P. J., Gizis J. E., 2012, *ApJ*, 746, 3
- Castro P. J., Gizis J. E., Gagné M., 2011, *ApJ*, 736, 67
- Chiba M., Beers T. C., 2000, *AJ*, 119, 2843
- Cooke A., Rodgers B., 2005, in Shopbell P., Britton M., Ebert R., eds, ASP Conf. Ser., Vol. 347, IRAF Package for GNIRS Data Reduction – A Product of the Gemini/NOAO Collaboration. Astron. Soc. Pac., San Francisco, p. 514
- Coşkunoğlu B. et al., 2011, *MNRAS*, 412, 1237
- Cruz K. L. et al., 2007, *AJ*, 133, 439
- Cushing M. C., Vacca W. D., Rayner J. T., 2004, *PASP*, 116, 362
- Cushing M. C. et al., 2011, *ApJ*, 743, 50
- Day-Jones A. C. et al., 2011, *MNRAS*, 410, 705
- Day-Jones A. C. et al., 2013, *MNRAS*, 430, 1171
- Delorme P. et al., 2008, *A&A*, 482, 961
- Dupuy T. J., Liu M. C., 2012, *ApJS*, 201, 19
- Elias J. H., Rodgers B., Joyce R. R., Lazo M., Doppmann G., Winge C., Rodríguez-Ardila A., 2006, in McLean I. S., Iye M., eds, Proc. SPIE Conf. Ser. Vol. 6269, Performance of the Gemini near-infrared spectrograph. SPIE, Bellingham, p. 626914
- Epchtein N. et al., 1999, *A&A*, 349, 236
- Faherty J. K., Burgasser A. J., Cruz K. L., Shara M. M., Walter F. M., Gelino C. R., 2009, *AJ*, 137, 1
- Faherty J. K., Rice E. L., Cruz K. L., Mamajek E. E., Núñez A., 2013, *AJ*, 145, 2
- Feltzing S., Bensby T., Lundström I., 2003, *A&A*, 397, L1
- Findlay J. R. et al., 2012, *MNRAS*, 419, 3354
- Fuhrmann K., 2000, in Bergeron J., Renzini A., eds, Proc. VLT Opening Symposium, From Extrasolar Planets to Cosmology. Springer, Berlin, p. 351
- Gauza B. et al., 2012, *MNRAS*, 427, 2457
- Geballe T. R. et al., 2002, *ApJ*, 564, 466
- Geballe T. R., Saumon D., Golimowski D. A., Leggett S. K., Marley M. S., Noll K. S., 2009, *ApJ*, 695, 844
- Gelino C. R. et al., 2011, *AJ*, 142, 57
- Gizis J. E., Burgasser A. J., Faherty J. K., Castro P. J., Shara M. M., 2011a, *AJ*, 142, 171
- Gizis J. E., Troup N. W., Burgasser A. J., 2011b, *ApJ*, 736, L34
- Gomes J. I. et al., 2013, *MNRAS*, 431, 2745
- Goodwin S. P., Whitworth A., 2007, *A&A*, 466, 943
- Griv E., Gedalin M., Eichler D., 2009, *AJ*, 137, 3520
- Hambly N. C. et al., 2008, *MNRAS*, 384, 637
- Hewett P. C., Warren S. J., Leggett S. K., Hodgkin S. T., 2006, *MNRAS*, 367, 454
- Irwin M. J. et al., 2004, *Proc. SPIE*, 5493, 411
- King R. R., McCaughrean M. J., Homeier D., Allard F., Scholz R.-D., Lodieu N., 2010, *A&A*, 510, A99
- Kirkpatrick J. D. et al., 1999, *ApJ*, 519, 802
- Kirkpatrick J. D. et al., 2011, *ApJS*, 197, 19 (K11)
- Kirkpatrick J. D. et al., 2012, *ApJ*, 753, 156 (K12)
- Kissler-Patig M. et al., 2008, *A&A*, 491, 941
- Lawrence A. et al., 2007, *MNRAS*, 379, 1599
- Leggett S. K. et al., 2000, *ApJ*, 536, L35
- Leggett S. K. et al., 2010, *ApJ*, 710, 1627
- Leggett S. K., Morley C. V., Marley M. S., Saumon D., Fortney J. J., Visscher C., 2013, *ApJ*, 763, 130
- Liebert J., Burgasser A. J., 2007, *ApJ*, 655, 522
- Liu M. C. et al., 2011, *ApJ*, 740, 108
- Lodieu N., Deacon N. R., Hambly N. C., 2012a, *MNRAS*, 422, 1495
- Lodieu N. et al., 2012b, *A&A*, 548, A53
- Lucas P. W. et al., 2010, *MNRAS*, 408, L56
- Mace G. N. et al., 2013, *ApJS*, 205, 6
- Machida M. N., Inutsuka S.-i., Matsumoto T., 2009, *ApJ*, 699, L157
- Mainzer A. et al., 2011, *ApJ*, 726, 30
- Marocco F. et al., 2010, *A&A*, 524, A38
- Mathis J. S., 1990, *ARA&A*, 28, 37
- Metchev S. A., Kirkpatrick J. D., Berriman G. B.,Looper D., 2008, *ApJ*, 676, 1281
- Nakajima T., Oppenheimer B. R., Kulkarni S. R., Golimowski D. A., Matthews K., Durrance S. T., 1995, *Nat*, 378, 463
- Nissen P. E., 2004, *Origin and Evolution of the Elements*. Cambridge Univ. Press, Cambridge, p. 154
- Pickles A. J., 1998, *PASP*, 110, 863
- Pinfield D. J., Jones H. R. A., Lucas P. W., Kendall T. R., Folkes S. L., Day-Jones A. C., Chappelle R. J., Steele I. A., 2006, *MNRAS*, 368, 1281
- Pinfield D. J. et al., 2008, *MNRAS*, 390, 304
- Pinfield D. J. et al., 2012, *MNRAS*, 422, 1922
- Rayner J. T., Cushing M. C., Vacca W. D., 2009, *ApJS*, 185, 289
- Rebolo R., Zapatero Osorio M. R., Martín E. L., 1995, *Nat*, 377, 129
- Reipurth B., Clarke C., 2001, *AJ*, 122, 432
- Reylé C. et al., 2010, *A&A*, 522, A112
- Saumon D., Marley M. S., 2008, *ApJ*, 689, 1327
- Saumon D., Bergeron P., Lunine J. I., Hubbard W. B., Burrows A., 1994, *ApJ*, 424, 333
- Schlegel D. J., Finkbeiner D. P., Davis M., 1998, *ApJ*, 500, 525
- Simcoe R. A. et al., 2008, in McLean I. S., Casali M. M., eds, Proc. SPIE Conf. Ser. Vol. 7014, FIRE: A Near-Infrared Cross-Dispersed

Echelle Spectrometer for the Magellan Telescopes. SPIE, Bellingham, p. 70140U
Simcoe R. A. et al., 2010, in McLean I. S., Ramsay S. K., Takami H., eds, Proc. SPIE Conf. Ser. Vol. 7735, The FIRE Infrared Spectrometer at Magellan: Construction and Commissioning. SPIE, Bellingham, p. 773514
Skrutskie M. F. et al., 2006, AJ, 131, 1163
Stamatellos D., Whitworth A. P., 2009, MNRAS, 392, 413
Strauss M. A. et al., 1999, ApJ, 522, L61
Tinney C. G., Faherty J. K., Kirkpatrick J. D., Wright E. L., Gelino C. R., Cushing M. C., Griffith R. L., Salter G., 2012, ApJ, 759, 60

Vacca W. D., Cushing M. C., Rayner J. T., 2003, PASP, 115, 389
Warren S. J. et al., 2007, MNRAS, 381, 1400
Wright E. L. et al., 2010, AJ, 140, 1868
York D. G. et al., 2000, AJ, 120, 1579
Zacharias N. et al., 2010, AJ, 139, 2184
Zhang Z. H. et al., 2010, MNRAS, 404, 1817

This paper has been typeset from a $\text{\TeX}/\text{\LaTeX}$ file prepared by the author.